*J. Fluid Mech.* (1998), *vol.* 357, *pp.* 83–122. Printed in the United Kingdom



# Mixing, structure and scaling of the jet in crossflow

By S. H. SMITH AND M. G. MUNGAL

Mechanical Engineering Department, Stanford University, Stanford, CA 94305-3032, USA

(Received 27 August 1996 and in revised form 17 September 1997)

The mixing of the round jet normal to a uniform crossflow is studied for a range of jet-to-crossflow velocity ratios, $r$, from 5 to 25. Planar laser-induced fluorescence (PLIF) of acetone vapour seeded into the jet is used to acquire quantitative two-dimensional images of the scalar concentration field. Emphasis is placed on $r = 10$ and $r = 20$ and a few select images are acquired up to $r = 200$. The Reynolds number based on the jet exit diameter, $d$, and the exit velocity varies from 8400 to 41 500. Images are acquired for conditions in which the product $rd$ is held constant, requiring decreasing $d$ for increasing $r$.

Results from this experimental study concern structural events of the vortex interaction region, and mixing and mean centreline concentration decay in the near and far fields. The results cover all three regions of the transverse jet, and suggest that the jet scales with three length scales: $d$, $rd$ and $r^2d$.

Events within the vortex interaction region display $d$-scaling, including the crossflow boundary layer separation and roll-up. Over the range of velocity ratios studied, the vortex interaction region shows $r$-dependent variations in the flow field, including the emergence of jet fluid in the wake structures for $r > 10$ and a slower development of the counter-rotating vortex pair (CVP) in higher-$r$ jets.

The trajectory and physical dimension of the jet in both the near and far field display $rd$-scaling. The near field is characterized by a centreline concentration decay along the centreline coordinate $s$ of $s^{-1.3}$, different from the decay rate ($s^{-1}$) of the free jet. When normalized by $rd$, the decay of each velocity-ratio jet branches away from the $s^{-1.3}$ decay, approaching a decay of $s^{-2/3}$, a rate predicted by modelling efforts. The branch points represent a transition in the flow field from enhanced mixing to reduced mixing compared to the free jet. When normalized by $r^2d$, the branch points occur at a uniform jet position, $s/r^2d = 0.3$, which is viewed to be the division between the near and far fields. Self-similarity is not seen in the near field, but may be present in the far field.

The view of the branch points as a place of transition in the flow is supported by the probability density function (p.d.f.) of concentration along the upper edge of the jet. Before the branch points, the p.d.f.s are non-marching in character, and after the branch points, they are tilted in character.

Instantaneously, the CVP is asymmetric in shape and concentration. End views reveal extensive motion of the CVP and plan views show this motion can occur in both axisymmetric and sinusoidal motion. Ensemble-averaged images show the jet concentration is asymmetric about the centreline plane.

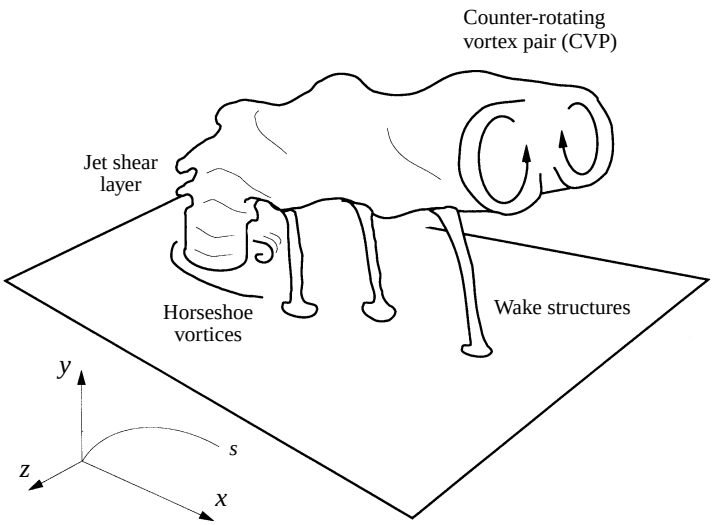


FIGURE 1. The known vortical structures of the jet in the crossflow, after Fric & Roshko (1994).

## 1. Introduction

The jet in crossflow has many practical technical applications, including use in primary combustion, overfire cooling, industrial mixing and emergency venting. The flow field can be witnessed issuing from the exhaust stacks of most power plants, and behind steam locomotives. In many of these applications, the resulting temperature downstream of the jet, the concentration of a hazardous material entering the crossflow from the jet, or the trajectory and physical path of the jet are important design parameters. These needs require quantitative evaluation of the jet fluid concentration, both instantaneous and ensemble-averaged, as it mixes with the crossflow fluid.

The results presented here are based solely on planar images of the instantaneous jet concentration, where the jet exit concentration is 100%. The instantaneous picture of the jet concentration field allows for both the identification and analysis of the jet structure and for the evaluation of statistically based quantities such as the maximum centreline concentration decay.

The flow field of the jet in crossflow depends primarily upon the ratio of the jet momentum to the crossflow momentum. It is customary to define the effective velocity ratio, $r$, as the square root of the momentum-flux ratio,

$$r = \left( \frac{\rho_j U_j^2}{\rho_{cf} U_{cf}^2} \right)^{1/2}. \tag{1.1}$$

In the case of equal-density flows, $r = U_j/U_{cf}$. Here $U$ is velocity; $\rho$ is density, and subscripts $j$ and $cf$ refer to jet properties and crossflow properties respectively.

The jet in crossflow consists of four known vortical structures shown in figure 1: the horseshoe vortices, the jet shear layer, the wake structures and the counter-rotating vortex pair (CVP) (Fric & Roshko 1994). The horseshoe vortices form upstream of the jet exit, wrapping around the exiting jet column. The jet shear layer consists of the ring vortices in the jet boundary. The wake structures form downstream of the jet column, and persist and convect far downstream of the exit nozzle. The jet column transitions to the CVP, the dominant vortical structure of the transverse jet after the jet has turned in the crossflow direction.

Analysis of the vortical structure of the transverse jet includes work focusing on the horseshoe vortex system (Krothapalli, Lourenco & Buchlin 1990; Kelso & Smits 1995), the wake vortex system (Fric & Roshko 1994; Kelso, Lim & Perry 1996; Eiff, Kawall & Keffer 1995; McMahon, Hester & Palfery 1971; Moussa, Trischka & Eskinazi 1977), and the vorticity dynamics of the exiting jet (Coelho & Hunt 1989; Needham, Riley & Smith 1988; Sykes, Lewellen & Parker 1986). Together, these authors establish that the horseshoe vortex system has oscillating modes that persist at the same Strouhal number as the wake vortices. For transverse jets issuing from a pipe extending into the crossflow, the wake vortices lock onto the shedding vortices behind the pipe (Eiff *et al.* 1995), and for jets injected flush with the wall, the Strouhal number based on the jet diameter closely matches the value obtained from a cylinder with the same diameter (Moussa *et al.* 1977). ($St = 0.15$ for $r = 2$ to $r = 8$, falling to $St = 0.06$ at $r = 20$). Note that all Strouhal numbers are based on the jet exit diameter, $d$.

Fric & Roshko (1994) identify two sources of vorticity in the jet in crossflow: the crossflow boundary layer, and the jet exit boundary layer. Using smoke-wire visualization, they provide evidence that it is the crossflow boundary layer which provides the vorticity of the wake structures. They identify separation events of the crossflow boundary layer, which form vortices attaching to the lee side of the jet, turning up and becoming the wake structures. The turning-up mechanism is also seen in tornadoes. Kelso *et al.* (1996) further classify these events based on variations in Reynolds number and velocity ratio, and Coelho & Hunt (1989) note that diffusion of vorticity from the jet into the wake is weak. The basis of the argument Fric & Roshko present is photographic evidence, and a Thwaites boundary layer calculation that predicts the crossflow boundary layer separation position in relation to the jet column of diameter $d$. Their argument is based on a local length scale, $d$, just as the Strouhal number measurements are.

The jet exit diameter is not the only length scale present in the jet in crossflow. Broadwell & Breidenthal (1984) consider the jet exit as a point source of momentum flux (thereby analysing a region far downstream of the jet nozzle) and conclude that the only global length scale is $rd$, the product of the velocity ratio and the jet exit diameter. The $rd$ length scale was used by Pratte & Baines (1967) to collapse the centreline trajectories of jets of different $r$, using the correlation

$$\frac{y}{rd} = A\left(\frac{x}{rd}\right)^m, \tag{1.2}$$

with $A = 2.05$ and $m = 0.28$ for $r = 5$ to $r = 35$ (Pratte & Baines used photographs of flood-lit jet-seeded smoke to define the centreline). The coordinates $x$, $y$ and $z$ are defined in figure 1, offset from the true origin centred at the jet exit. Jet trajectory is still most often correlated by a functional form based on jet diameter, $y/d = A(r)^n(x/d)^m$; a good summary is provided by Margason (1993). The Pratte & Baines formulation reveals the utility of the $rd$ length scale for comparing jets with different $r$. Pratte & Baines, in fact, normalize distances in the jet using the $rd$ length scale, declaring that the far field of the transverse jet begins at $x = 3.2\,rd$.

A third length scale, $r^2d$, was used by Keffer & Baines (1963) to collapse jet trajectory data for $r = 6$, $r = 8$ and $r = 10$ up to 8 jet diameters from the jet exit.

Previous results on two additional topics, centreline concentration decay and self-similarity, are relevant to this discussion. Maximum centreline concentration decay results have been presented by Patrick (1967), Broadwell & Breidenthal (1984) and Hasselbrink & Mungal (1996). Patrick (1967) identifies a maximum centreline

concentration decay proportional to $s^{-1.2}$; his results extend directly from the jet exit. The Broadwell & Breidenthal (1984) model predicts a far-field decay proportional to $x^{-2/3}$, a result matched by Hasselbrink & Mungal (1996), using simple algebraic expressions derived from conservation of mass and momentum. The analysis of Hasselbrink & Mungal (1996), and to a lesser extent that of Broadwell & Breidenthal (1984), relies upon the jet obtaining self-similarity through a range of velocity ratio, $r$. Temperature profiles in the $z = 0$ plane have been shown to collapse to a Gaussian error curve using the functional form $(T - T_o)/(T_{max} - T_o)$ based on distances $y$ normalized by the half-width at half maximum (Kamotani & Greber 1972). Here $T_o$ is the crossflow temperature, $T_{max}$ the local maximum jet temperature, and $T$ the local jet temperature. Velocity profiles have also been shown to collapse using $(U - U_o)/(U_{max} - U_o)$ (Keffer & Baines 1963), where $U_o$ is the crossflow velocity, $U_{max}$ the local maximum jet velocity, and $U$ the local jet velocity. Neither Kamotani & Greber (1972) nor Keffer & Baines (1963) conclude that the transverse jet is a self-similar flow. Keffer & Baines (1963) and Patrick (1967) state that the transverse jet does not achieve self-similarity, while Chassaing *et al.* (1974) refer to the far-field region as the zone of velocity profile similarity.

The possibility of self-similarity is in direct contrast to a growing body of evidence that the transverse jet shows evolving characteristics which depend upon $r$. Kelso *et al.* (1996) define different vortical interactions at the nozzle depending upon velocity ratio (and Reynolds number). Similarly Fric & Roshko (1994) focus on the $r = 4$ jet because the bursting of the boundary layer fluid into the wake structures is most pronounced there. At low values of $r$, Andreopoulos & Rodi (1984) present the $r = 0.5$ jet as a flow that, downstream of the jet exit, re-entrains into the boundary layer with no memory of the jet. This is certainly not the case in the range from $r = 5$ to $r = 25$ studied here.

This work presents the experimental results from an extensive study of the concentration field of the jet in crossflow. The instantaneous images obtained show the vortical structure of the jet, and statistical quantities derived from these images reveal further insights. The results concern both the vortex interaction region of the jet and the jet near and far field. They are unified by an analysis and presentation of the length scales affecting the flow field. In § 2, the experimental methods will be presented, and in § 3 the run conditions are discussed. Section 4 will present results from the jet trajectory and structure, and § 5 will propose an extension to the Fric–Roshko mechanism to explain the presence of jet fluid in the wake structures. Section 6 will show the maximum centreline concentration measurements; § 7 the related p.d.f. results. The discussion will end with conclusions in § 8. Full details on all aspects of this work can be found in Smith (1996).

## 2. Experimental methods

This section describes the experimental techniques used to acquire planar images of the jet concentration field.

### 2.1. *Facility*

All images are acquired in a vertical wind tunnel, figure 2, designed and built specifically for PLIF studies. The tunnel consists of three sections: an inlet, a test section, and an exhaust section. The inlet section turns and conditions the flow field, yielding a smooth test section crossflow. It consists of a single radius contraction followed by three screens, honeycomb (0.317 cm cell diameter, 1.27 cm thick), and a

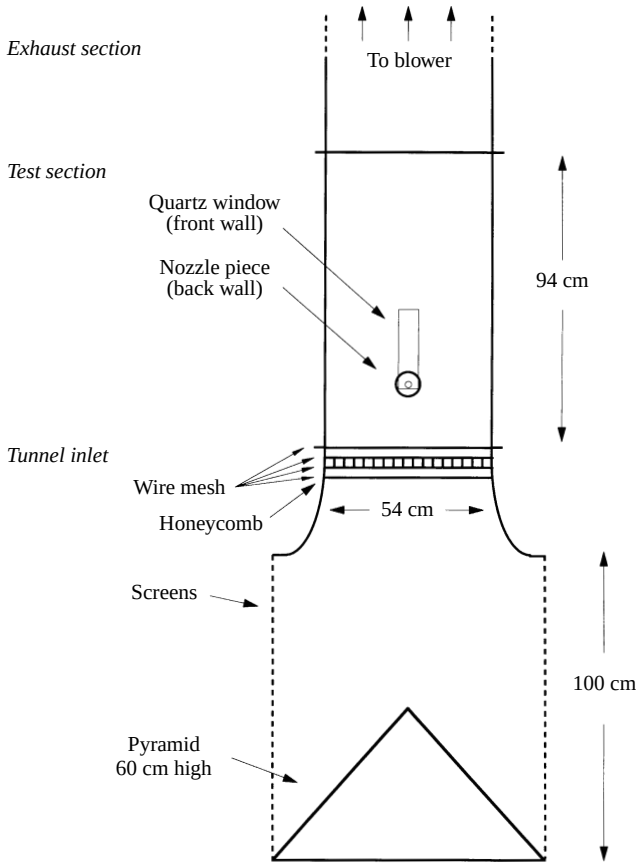


FIGURE 2. Flow facility schematic.

final screen (63% open area, 32 mesh per in.). The tunnel crossflow is sensitive to the uniformity of the final screen, and care is taken in its selection and maintenance. Common household screens (15 mesh per in.) and a 60 cm high 4-sided pyramid aid in turning the flow upward into the tunnel.

Hot-wire measurements are used to characterize the tunnel crossflow. It has an average velocity of 5.0 m $s^{-1}$ (which varies spatially across the tunnel less than 5 %), and a turbulence intensity of 0.8 %. The statistics are based on more than 400 data locations spread uniformly throughout the tunnel; the regions near the jet flow are carefully checked for flow non-uniformity, and none is present.

The tunnel test section is 54 cm by 54 cm and 94 cm in length. The jet is placed flush with the tunnel wall (20 cm above the final screen) using a jet plenum and removable nozzle block shown in figure 3. Perforated plate and honeycomb sections are placed in the plenum to ensure uniform jet flow. A pressure transducer and type K thermocouple are used to record pressure and temperature for run-time flow measurements. The use of the removable nozzle block allows quick changes in nozzle diameter. The nozzle diameters available (and their design velocity ratio) are 20 mm ($r = 2.5$; not studied), 10 mm ($r = 5$), 5 mm ($r = 10$), 3.3 mm ($r = 15$), 2.5 mm ($r = 20$) and 2.0 mm ($r = 25$).

The exhaust section maintains the same tunnel cross-section for another 94 cm, ensuring the test section is not affected by the connection to a round exhaust duct.

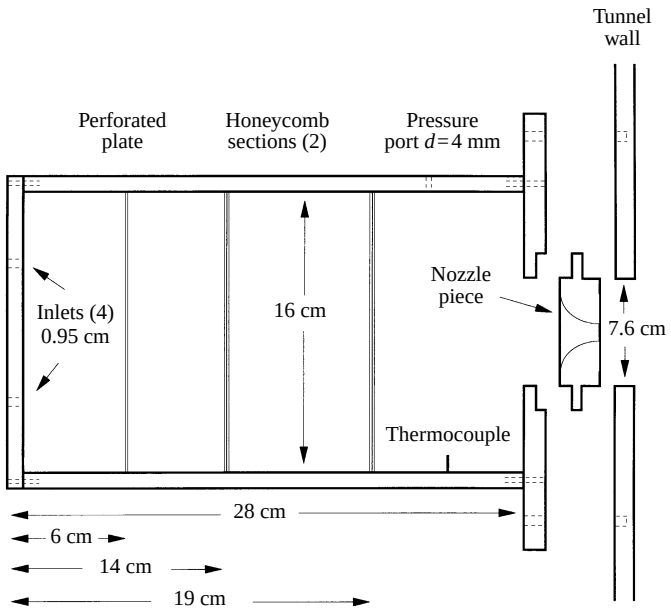


FIGURE 3. The jet plenum arrangement.

The tunnel is powered by a 5 h.p. centrifugal blower, 10 m downstream of the exhaust section. The exhaust section also provides optical access for end-view imaging.

### 2.2. *Planar laser-induced fluorescence*

Images of the concentration field are obtained using planar laser-induced fluorescence (PLIF), a non-intrusive optical diagnostic technique. Comprehensive treatments are given by Hanson (1988) and Eckbreth (1988); only a brief review will be presented here. PLIF uses a monochromatic light source that is formed into a sheet and passed through a flow field. The light source excites an energy transition in a chosen marker species, which fluoresces upon relaxation. The fluorescence is captured on an imaging array. PLIF can be used to quantitatively measure molecular number density (and thereby density, concentration and mixture fraction), temperature, pressure and velocity.

Acetone vapour is the current tracer of choice for concentration studies in turbulent flow fields at room temperature and pressure. Acetone fluorescence is a linear function of both incident laser energy and acetone concentration and no self-quenching occurs (Lozano, Yip & Hanson 1992). Room air can be used with acetone fluorescence because its fluorescence is not quenched by $O_2$, as is the case for phosphorescence of biacetyl. Also, acetone absorbs in the uv (225–320 nm; 278 nm peak) and emits in the visible (350–550 nm, 435 nm peak), allowing for the use of non-gated, non-intensified CCD arrays, giving high dynamic range (upwards of 200) and high signal to noise (upwards of 200) images.

In the current experiment, PLIF is used exclusively to measure concentration of the jet fluid as shown schematically in figure 4. A XeCl excimer laser provides a 400 mJ, 308 nm pulse which is formed into a sheet ($f = 75$ mm cylindrical lens) and focused to a waist ($f = 1$ m lens) in the test section. The sheet thickness is 0.6 mm in the measured flow field regions. The jet flow is seeded with acetone vapour ($\sim 10$ % by

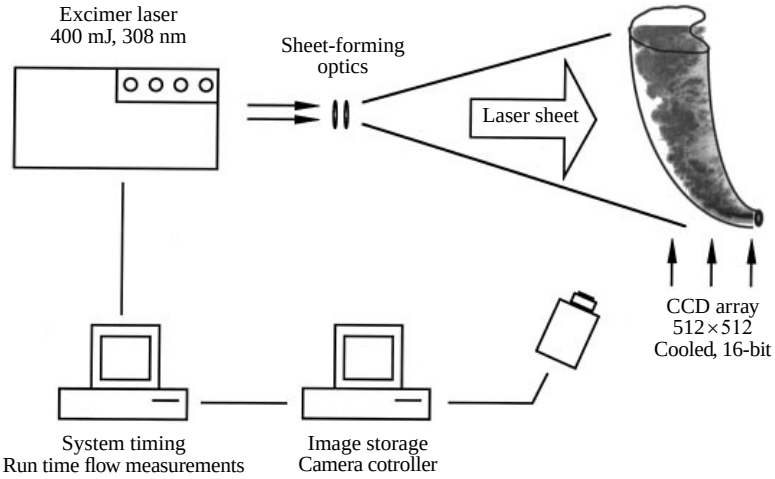


FIGURE 4. PLIF imaging systems.

volume) by bubbling filtered air through two pressurized cylinders (in series, 10 cm diameter) filled 20 cm deep with liquid acetone. Bypass air is used for low-volume-flux cases to ensure that condensation at the nozzle lip does not occur, as witnessed in preliminary data. Heating tape applied to the jet plenum ensures the exit temperature of the jet is equal to the crossflow temperature, a necessary condition for the number density of acetone molecules to map uniformly to jet concentration. A 512 by 512 pixel CCD array images the fluorescence. The camera is non-intensified, thermoelectrically cooled (−40 °C), and has 16-bit pixel resolution.

Each image is individually corrected for background levels, laser sheet non-uniformities and laser absorption. Absorption of the laser energy follows the Beer–Lambert law. Absorption corrections for experiments with collimated sheets are available (Clemens 1991; Karasso 1994). However, the large imaging area (25 cm by 25 cm) in this experiment required the use of an expanding laser sheet; numerical details of a Beer–Lambert correction using an expanding sheet are found in Smith (1996).

Final values of concentration are established by setting the jet potential core values to $C = 100\,\%$. End- and plan-view images do not contain the potential core, so the concentration values are established by comparing the common line of data from the ensemble-averaged plan or end view and the appropriate ensemble-averaged side view. Similarly, the $d = 3.3$ mm, $d = 2.5$ mm and $d = 2.0$ mm nozzles are not large enough to produce a potential core region where 10–20 pixels are completely filled with pure jet fluid. The concentration in these cases is established by comparing ensemble-averaged images from data of the same $r$, using $d = 5.0$ mm.

For mixing measurements, the most important criterion in designing a PLIF set-up is the image resolution. The laser sheet thickness (0.6 mm) sets the minimum resolution, and the camera must be placed so each pixel measures a value close to the sheet thickness. In this experiment all side and plan views use a pixel width which measures 0.51 mm at the imaging plane. Resolution cannot be improved by moving the camera closer to the imaging plane.

| | | | | | Jet | | Crossflow | |
|---|---|---|---|---|---|---|---|---|
| $r$ | $Re_j$ | $rd$ | $U_{cf}$ | $d$ | $\delta_1$ | $\theta$ | $\delta_1/d$ | $\theta/d$ |
| - | - | (mm) | (m s$^{-1}$) | (mm) | (mm) | (mm) | - | - |
| 5 | 16 600 | 50 | 5.0 | 10 | 0.15 | 0.06 | 0.11 | 0.06 |
| 10 | 16 600 | 50 | 5.0 | 5 | 0.10 | 0.04 | 0.22 | 0.11 |
| 10 | 33 000 | 100 | 5.0 | 10 | 0.10 | 0.05 | 0.11 | 0.06 |
| 15 | 16 600 | 50 | 5.0 | 3.3 | 0.07 | 0.04 | 0.33 | 0.17 |
| 15 | 25 000 | 75 | 5.0 | 5 | 0.07 | 0.04 | 0.22 | 0.11 |
| 20 | 16 600 | 50 | 5.0 | 2.5 | 0.06 | 0.04 | 0.44 | 0.22 |
| 20 | 33 000 | 100 | 5.0 | 5 | 0.07 | 0.04 | 0.22 | 0.11 |
| 25 | 16 600 | 50 | 5.0 | 2.0 | 0.06 | 0.03 | 0.55 | 0.28 |
| 25 | 41 500 | 125 | 5.0 | 5 | 0.07 | 0.04 | 0.22 | 0.11 |
| 10 | 33 000 | 200 | 2.5 | 20 | 0.16 | 0.06 | 0.10 | 0.04 |
| 20 | 33 000 | 200 | 2.5 | 10 | 0.10 | 0.05 | 0.18 | 0.07 |

TABLE 1. Tunnel run conditions. $\delta_1$ is the boundary layer displacement thickness, $\theta$ the momentum thickness.

## 3. Run conditions

In this experiment, the $rd$ length scale is held constant through a range of velocity ratios. The effect is accomplished by changing the nozzle diameter, $d$, for each change in velocity ratio, $r$. The camera is held at a fixed distance throughout the entire data set, due to the resolution limitations of the laser sheet. Increasing $d$ at a fixed $r$ has the effect of magnifying the imaged region, but the magnification is caused by an increase in physical dimensions.

Data sets in this experiment consist of 400 images each for side and end views and 300 images each for plan views. Side-view data sets are acquired at $r = 5$ ($d = 10$ mm), $r = 10$ ($d = 5$ mm, 10 mm), $r = 15$ ($d = 3.3$ mm, 5 mm), $r = 20$ ($d = 2.5$ mm, 5 mm) and $r = 25$ ($d = 2.0$ mm, 5 mm), as shown in table 1. Each side-view case is imaged at two nozzle diameters. The first gives an image where $rd = 50$ mm (an image width of $5\,rd$, and $Re_j = 16\,600$) and the second gives a magnified data set ($2\,rd$ to $3.3\,rd$ wide, depending upon the case). Smaller sets of 10 to 50 images are acquired for $r = 5$ to $r = 200$. End- and plan-view images are acquired at $r = 10$ and $r = 20$ to allow for imaging in multiple planar locations, shown in figure 5.

Keeping $rd$ constant holds $Re_j$ constant as well, but the different jet diameters used changes the relative sizes of the jet boundary layer, crossflow boundary layer and jet exit diameter. Boundary layer characteristics of both the (non-interacting) jet and crossflow are calculated using STAN7, a boundary layer code (Crawford & Kays 1976). Transition to turbulent boundary layers is assumed to occur at a momentum thickness Reynolds number of 162. Table 1 summarizes the tunnel conditions at each case. All displacement and momentum thicknesses are presented at the position of the jet exit. The combination of $r$ and $Re_j$ uniquely identifies all cases with $U_{cf} = 5.0$ m s$^{-1}$. Two cases with $U_{cf} = 2.5$ m s$^{-1}$ are included, corresponding only to the ensemble-averaged plan views to be shown.

### 3.1. *Resolution and signal-to-noise ratio*

The fidelity of the images acquired depends upon the image resolution and the signal-to-noise ratio. The finest scalar fluctuations occur at the Batchelor scale, $\lambda_B = \beta\delta Re_\delta{}^{-0.75} Sc^{-0.5}$, where $\delta$ is the local jet width, $\beta$ a constant, $Re_\delta$ the Reynolds

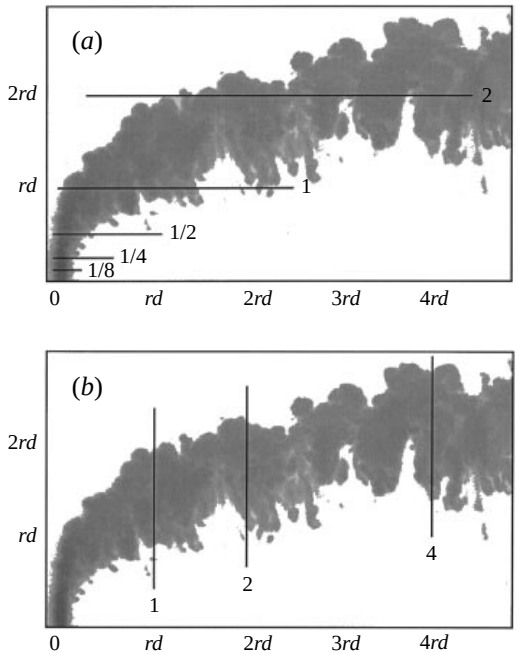


FIGURE 5. Imaging planes for (*a*) plan views and (*b*) end views.

| $r$ | $x = rd$ | $x = 4\,rd$ |
|---|---|---|
| 5 | 70 | 47 |
| 10 | 56 | 37 |
| 15 | 43 | 25 |
| 20 | 39 | 22 |
| 25 | 25 | 13 |

TABLE 2. A summary of signal to noise ratio.

number based on the local jet velocity and width, and $Sc$ the Schmidt number. Measurements in a free jet by Dowling & Dimotakis (1990) suggest $\beta \approx 25$. Following the work of Clemens & Mungal (1995) and Karasso & Mungal (1996), a figure of merit $L/\lambda_B$ will be used to characterize the ability of an image to resolve the finest scales of mixing. $L$ is the largest probe dimension, and $\lambda_B$ is the Batchelor scale, with $\beta = 1$. Thus $L/\lambda_B$ values of less than 25 may be considered resolved.

The $L/\lambda_B$ values in this experiment lie between 10.0 and 13.7 for end- and side-view images. The local Reynolds number in the transverse jet decreases with $s$; these values are based on the jet exit Reynolds number making the $L/\lambda_B$ values a conservative estimate. Side-view images are only resolved for regions where $x > rd$ because the jet width must grow to a sufficient size. The ability of plan views to resolve the Batchelor scale is not considered because they are not used in mixing statistics.

The signal-to-noise ratio (SNR) describes the camera's ability to recreate the fluorescence image. SNR varies spatially across the image, with higher values occurring in regions of higher acetone concentration. Typical SNR values in the jet near and far field range from 13 to 70 and are listed in table 2 at two downstream locations.

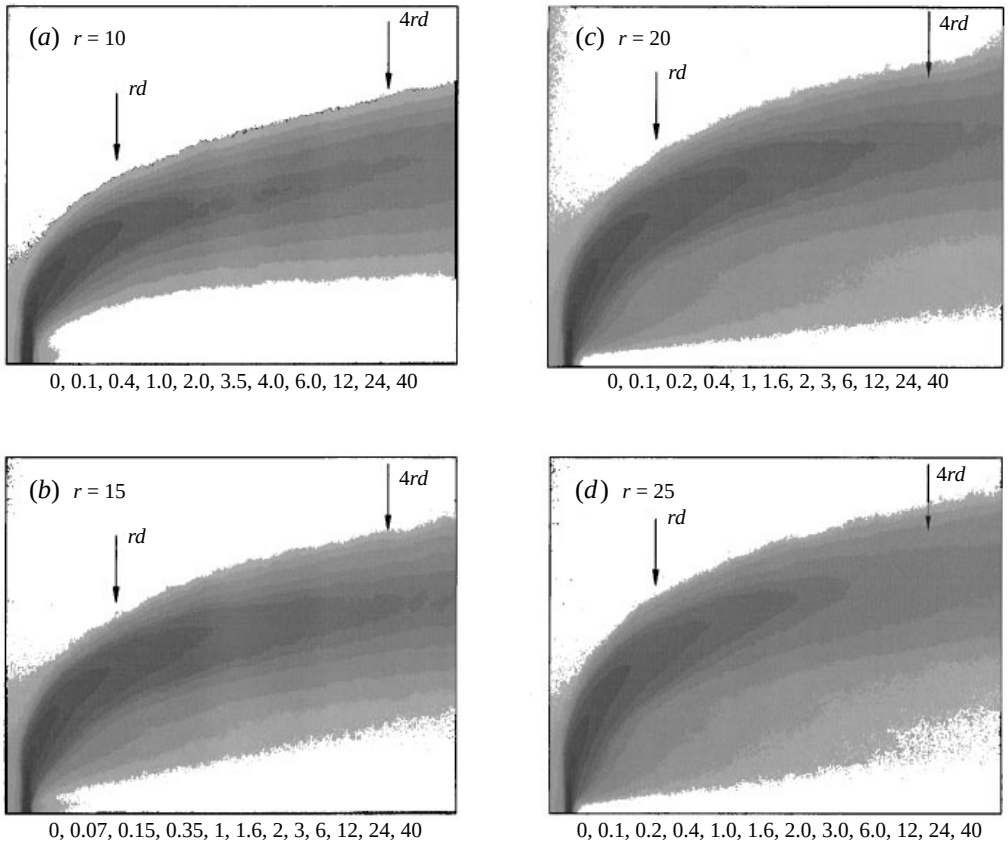


FIGURE 6. Side-view ensemble-averaged concentration fields for (*a*) $r = 10$, (*b*) $r = 15$, (*c*) $r = 20$, and (*d*) $r = 25$. $Re_j = 16\,600$ and image frame is $5\,rd$ by $4\,rd$ in all cases. Contour levels are given below each image in percent jet fluid concentration.

## 4. Jet trajectory and structure

The instantaneous images and the ensemble average acquired for each data set are used to obtain trajectory, structure and scaling data. These results are presented in this section.

### 4.1. *Trajectory and scaling of physical dimensions*

The jet trajectory presented here is defined to be the locus of points in the $z = 0$ plane at which the maximum concentration value occurs in a line perpendicular to the local jet direction. Thus this trajectory is based upon local maximum mean concentration, and not upon velocity measurements. Kamotani & Greber (1972) and Haniu & Ramaprian (1989) show that the trajectory based on maximum local velocity penetrates 5–10% deeper ($+y$) into the flow than the corresponding scalar concentration trajectory.

Trajectory data are obtained from the ensemble-averaged contour plots of the side-view images shown in figure 6, where each average is obtained from 400 instantaneous images acquired at the same tunnel run conditions. Each image is shown in a frame $5\,rd$ wide and $4\,rd$ high.

Trajectory data are displayed in figure 7 for $r = 5$ to $r = 25$ using the $rd = 50$ mm data. The $x$- and $y$-coordinates in the trajectory plot are normalized by the length

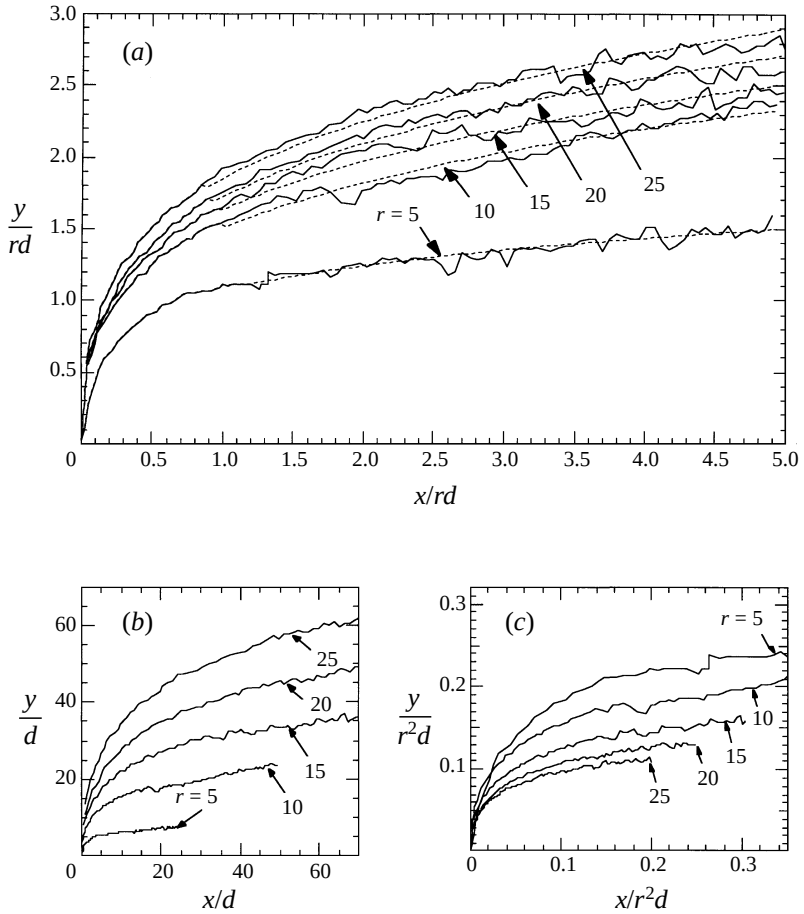


FIGURE 7. Centreline jet trajectory normalized by (*a*) $rd$, (*b*) $d$ and (*c*) $r^2d$.

scale $rd$ in figure 7(*a*), and for comparison plots normalized by $d$ (figure 7*b*) and $r^2d$ (figure 7*c*) are included. The $d$-scaled plot shows that the jet penetration increases with increasing $r$, and as expected the $r = 5$ jet does not penetrate into the crossflow as deeply as the $r = 25$ case. The $r^2d$ length scale clearly does not collapse the trajectory profiles of jets with different $r$. The trajectory plot given by Keffer & Baines (1963) showed similar trajectories for $r = 6$, $r = 8$ and $r = 10$ to $x/r^2d = 0.05$ only, and the $r = 5$ and $r = 10$ jets in this data set do converge in that limited range.

The $rd$-scaled trajectories, figure 7(*a*), do not collapse completely, as the data of Pratte & Baines (1967) do. The difference may result because the Pratte & Baines (1967) data extend to $100\,rd$ and are acquired using a pipe that extends into the crossflow. The use of a jet flush with the tunnel wall may cause an $r$-dependent low-pressure region behind the jet exit which affects the trajectory. Fric & Roshko (1994) identify a low-pressure region for $r \leqslant 8$ but these results are likely not to be representative of the higher velocity ratio regime. To date there are no pressure measurements near the jet exit for velocity ratios from 10 to 25. The best fit of the trajectory data in figure 4 gives values of $A = 1.5$ and $m = 0.27$ in the Pratte & Baines formulation, equation (1.2).

The advantage of normalizing by $rd$ instead of $d$ or $r^2d$ is also apparent when the

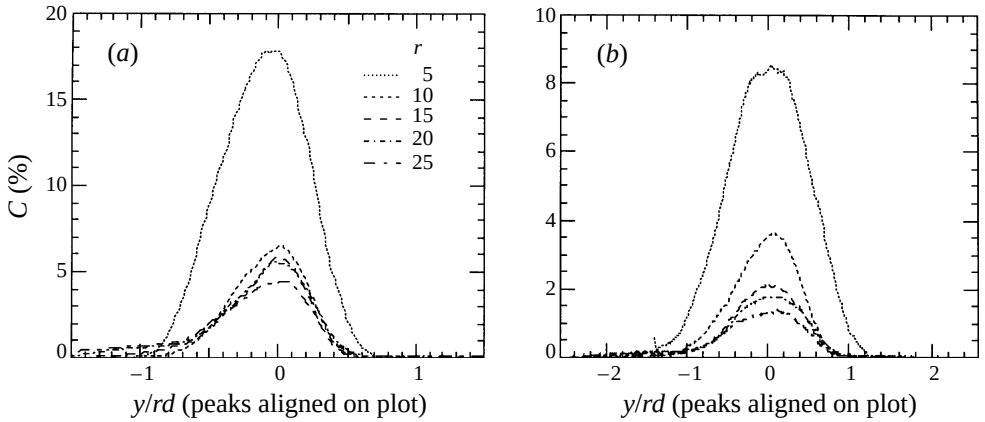


FIGURE 8. Concentration profiles of ensemble-averaged jets, (*a*) $x = rd$, (*b*) $x = 4rd$. $Re_j = 16\,600$ and $z = 0$ for all cases.

physical dimensions of the jet are considered. Ensemble-averaged contour plots of the $r = 10$, $r = 15$, $r = 20$ and $r = 25$ were displayed in figure 6. Profiles of the ensemble-averaged concentration at $x = rd$ and $x = 4rd$ are shown in figure 8. The profiles reveal that up to a factor of 5 difference in $r$ (5 to 25), the jet dimension scales with $rd$, and the jet height ($y_{max} - y_{min}$) is equal to approximately $2rd$ at $x = 4rd$ downstream.

The best evidence that the jet size scales with $rd$ is the end-view ensemble-averaged contour images, figure 9, which show the $r = 10$ and $r = 20$ cases at $x = rd$, $x = 2rd$ and $x = 4rd$. These images clearly show the CVP of each jet. The physical dimensions of these two jets at the same $x/rd$ are seen to be essentially the same.

The low-concentration region ($\approx 0.1\%$) below the $r = 15$ and $r = 20$ jets, figure 6, are the result of jet fluid in the wake structures, an issue to be discussed in § 5 after instantaneous images are considered. This effect is also seen in figure 9, occurring as a finger of jet fluid pointing from the jet body to the tunnel wall for the $r = 20$ case.

4.1.1. *Jet asymmetry*

The ensemble-averaged end views, figure 9, also reveal that the jet concentration imaged in this experiment is not symmetric about the $z = 0$ plane. Symmetry in the jet in crossflow has not been previously discussed, except by Kuzo (1995), and has been implicitly assumed by previous researchers. The results from this study cannot confirm whether the jet in crossflow is a symmetric flow or not, but the possibility that the flow is not symmetric needs to be considered.

In this experiment, multiple planes are imaged for an array of tunnel conditions, with days often passing between runs of the same tunnel set-up. In every case, the asymmetry seen in the ensemble-averaged images remained the same in degree and direction. The crossflow is carefully checked for asymmetry (none is found), and care is taken to ensure uniform flow from the jet plenum. Cylindrical uniformity of the exit nozzles is checked, and they are accurate to 0.005 cm. The jet plenum, figure 3, contains flow conditioning devices to ensure a uniform jet exit, although nozzle diameters are typically too small to allow jet exit plane velocity measurements to be obtained with hot-wire anemometry. In brief, the experimental set-up is symmetric to laboratory accuracy, but the jet imaged is not symmetric. The worst case of asymmetry found is the $r = 20$ jet at $x = 4rd$, figure 9($f$); in that case the peak concentration

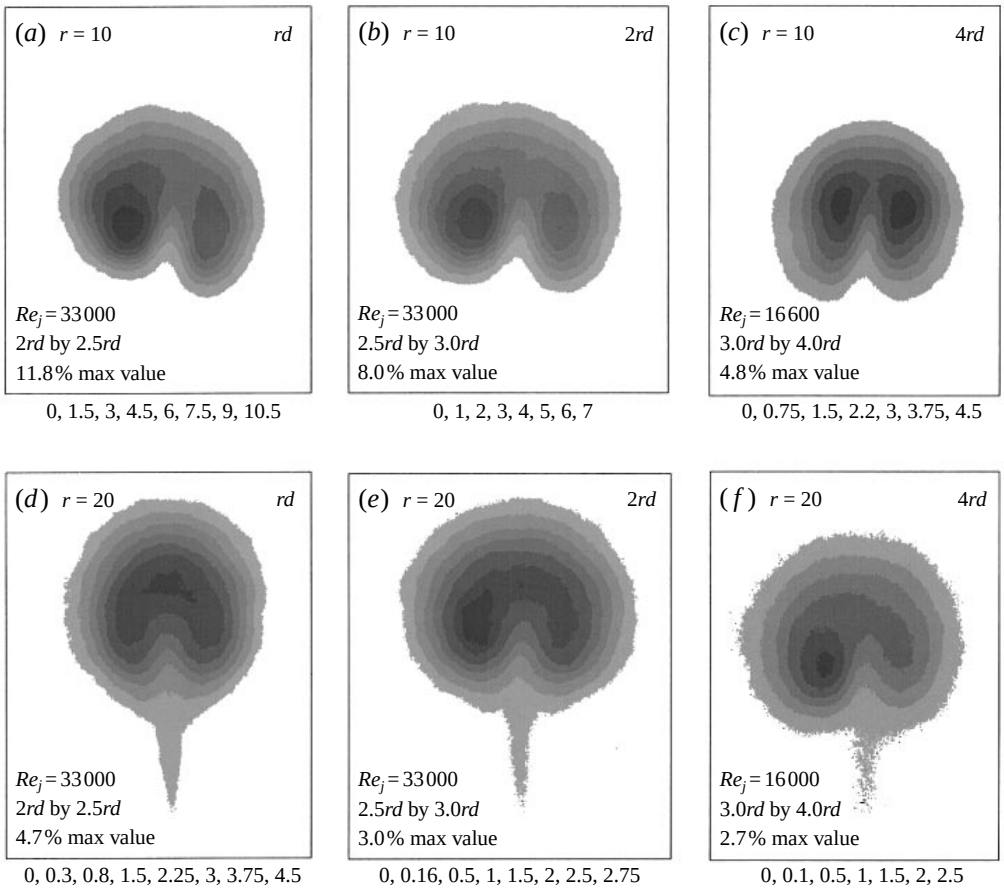


FIGURE 9. Ensemble-averaged end-view concentration fields for $x = rd$, $2rd$ and $4rd$. Contour levels are listed below each case, given in % concentration of initial jet fluid. $Re_j$, frame size and maximum concentration are given for each case. (*a–c*) $r = 10$; (*d–f*) $r = 20$.

in the $z > 0$ region is twice that of the $z < 0$ region. Images (*d*) and (*e*) from figure 9 are from the same tunnel conditions. In this case, the asymmetry does not develop until after $x = rd$ (although very slight asymmetry is seen in figure 9*d*).

A literature review reveals a growing body of experimental work where the average concentration profile is asymmetric about the $z = 0$ plane. Kamotani & Greber (1972) show temperature profiles from an $r = 7$ jet at distances of $3\,d$, $15\,d$ and $70\,d$ downstream of the jet exit. The $3\,d$ average is symmetric, while the $15\,d$ and $70\,d$ averages are not. Asymmetries are also seen in the work of Eiff (1996), McCann & Bowersox (1996) and Liscinsky, True & Holdeman (1996). The only author to discuss asymmetry is Kuzo (1995), who presents end-view particle image velocimetry results, and shows that asymmetry occurs below a cut-off Reynolds number. The overall findings of several researchers, except Kuzo (1995), point to increasing asymmetry with increasing $r$ and increasing distance downstream.

This body of evidence is not large because often symmetry is assumed. Computational investigations employ boundary conditions and grids that cover only half the flow field (Kim & Benson 1992; Sykes *et al.* 1986), and laboratory efforts display only

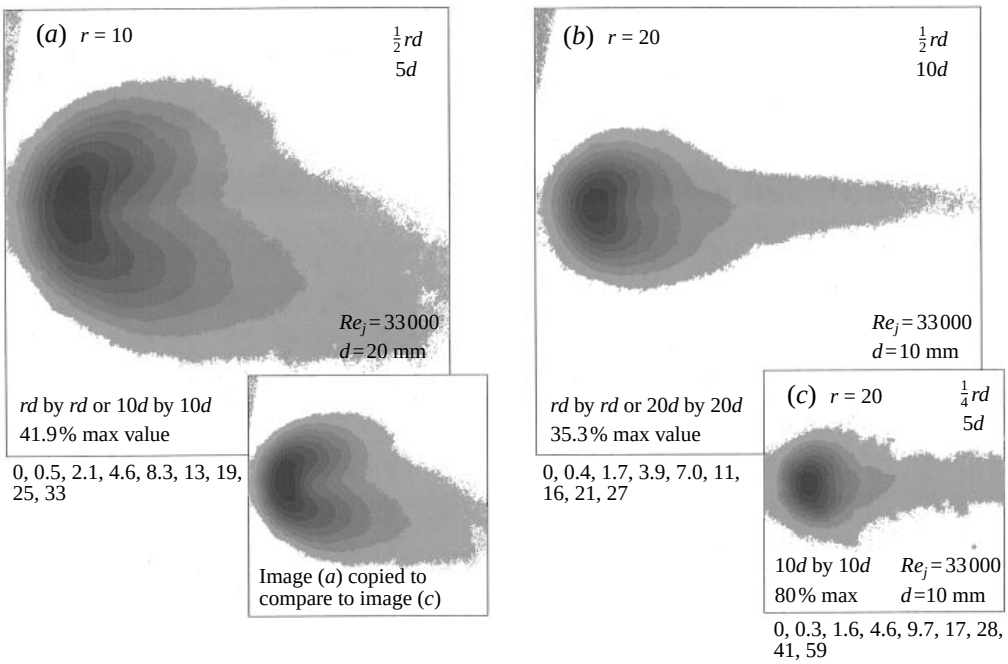


FIGURE 10. Ensemble-averaged plan-view images of jet concentration. (*a*) $r = 10$, (*b*, *c*) $r = 20$.

half the flow field (Andreopoulos & Rodi 1984; Moussa *et al.* 1977; Crabb, Durão & Whitelaw 1981; Sherif & Pletcher 1991; Fearn & Weston 1974).

It should be noted that as a practical matter, an experimentalist can place a jet into a crossflow only to within machining tolerances. Whether or not there is a perfectly arranged nozzle alignment that will create a symmetric flow is not yet known.

### 4.1.2. *CVP development*

The ensemble-averaged end views in figure 9 also show an important structural difference between the $r = 10$ and $r = 20$ jets. The CVP development in the $r = 20$ jet occurs farther downstream in $rd$-space than the CVP development in the $r = 10$ jet. CVP development refers to a progression from a circular jet exit, to an oval deformation, to a kidney shape, and finally to the position where the peak local jet concentration moves off the centreline ($z = 0$) plane. Different formation rates are evident from the end-view averages at $x = rd$; the $r = 20$ jet still has its maximum concentration value along the centreline, while the $r = 10$ jet has its maximum values off centreline in or near the CVP cores. The delayed CVP development in the 20:1 jet is seen in ensemble-averaged plan-view images shown in figure 10. Figure 10(*a*) shows the $y = \frac{1}{2}rd$ (or $y = 5\,d$) plane of the $r = 10$ jet. For comparison, (*b*) shows the $r = 20$ jet at $y = \frac{1}{2}rd$, and (*c*) shows the $r = 20$ jet at $y = 5\,d$. It is clear that the $r = 10$ jet shows a kidney shape consistent with development of the CVP that is much further progressed than either $r = 20$ case. In fact the higher $r = 20$ jet concentration contours are still oval shaped. The $r = 10$, $y = 5\,d$ image shown in figure 10 adds to the work of Coelho & Hunt, who present data for $r = 10$ at $y = 3\,d$ and $y = 4\,d$.

Note that the plan views shown in figure 10 are near enough to the jet nozzle that the jet size no longer scales strictly on $rd$. This is a result of the transition from a local scaling on $d$ in the vortex interaction region to an $rd$ scaling further downstream.

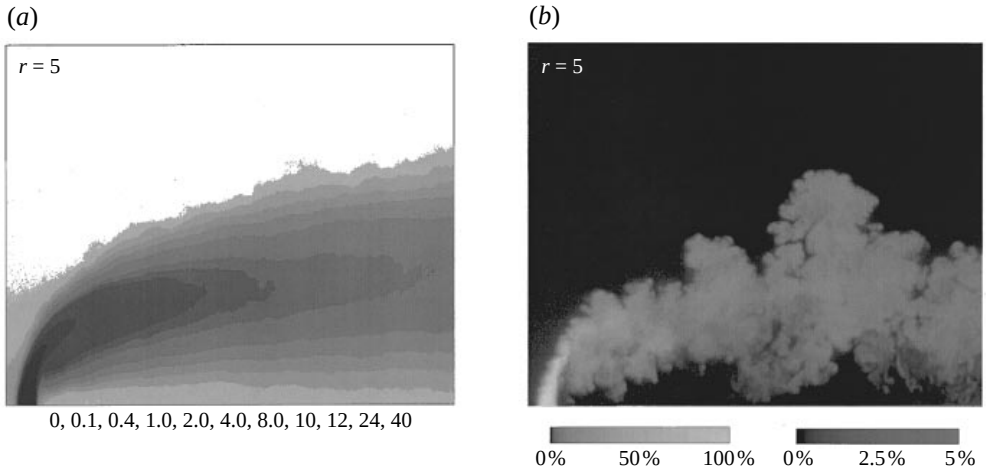


FIGURE 11. The presence of jet fluid near the tunnel wall for the $r = 5$ jet is shown in both the (*a*) ensemble-averaged image and (*b*) an instantaneous image. Both images are 5 *rd* by 4 *rd*. $Re_j = 16\,600$.

It is important to remember that the *rd* scaling is accomplished by changing the jet diameter; this implies that in images employing the same *rd* length scale, for example figures 10(*a*) and 10(*b*), the $r = 10$ jet exit diameter is twice that of the $r = 20$ jet exit diameter. The transition from *d*-scaling to *rd*-scaling is the reason the $r = 20$, $y = \frac{1}{2}rd$ plan view plane is smaller than the $r = 10$ plane also at $y = \frac{1}{2}rd$.

#### 4.1.3. *The $r = 5$ jet*

The side-view images of the $r = 5$ jet in figure 11 show that it never truly separates from the wall, yielding an average concentration of jet fluid at the wall equal to approximately 0.1%. An instantaneous image, figure 11(*b*), reveals that this average is the result of 1% concentration jet fluid occurring intermittently at the wall. It is the lack of true separation from the tunnel wall that initially leads us to believe the $r = 5$ jet belongs to a different regime of jets in crossflow than the $r = 10$ to $r = 25$ jets, probably due to wall effects best modelled by image vortices. This issue will be explored further as different results are presented.

### 4.2. *Instantaneous jet structure*

Instantaneous realizations of the jet concentration field are very different from the corresponding ensemble-averaged fields. Figure 12 shows a typical instantaneous side-view image through the $z = 0$ plane of an $r = 10$ jet. Concentration profiles through the jet are shown at five locations; the ensemble-averaged profiles are included on each instantaneous profile. The average is characterized by a smooth shape, which is Gaussian when sliced perpendicularly to the jet direction, while the instantaneous profiles are marked by sharp vertical rises in concentration resulting in small plateaus of high concentration fluid. The Gaussian-shaped average is a result of the unsteady dynamic motion of the high concentration regions.

The side-view image, figure 12, shows that free-stream fluid penetrating deeply into the jet. Penetrations from the upper edge occur almost to the jet centreline; penetration from the lower edge occurs to the centreline. These free-stream penetrations, especially from the upper edge, and the sharp rises in the instantaneous jet concentration field

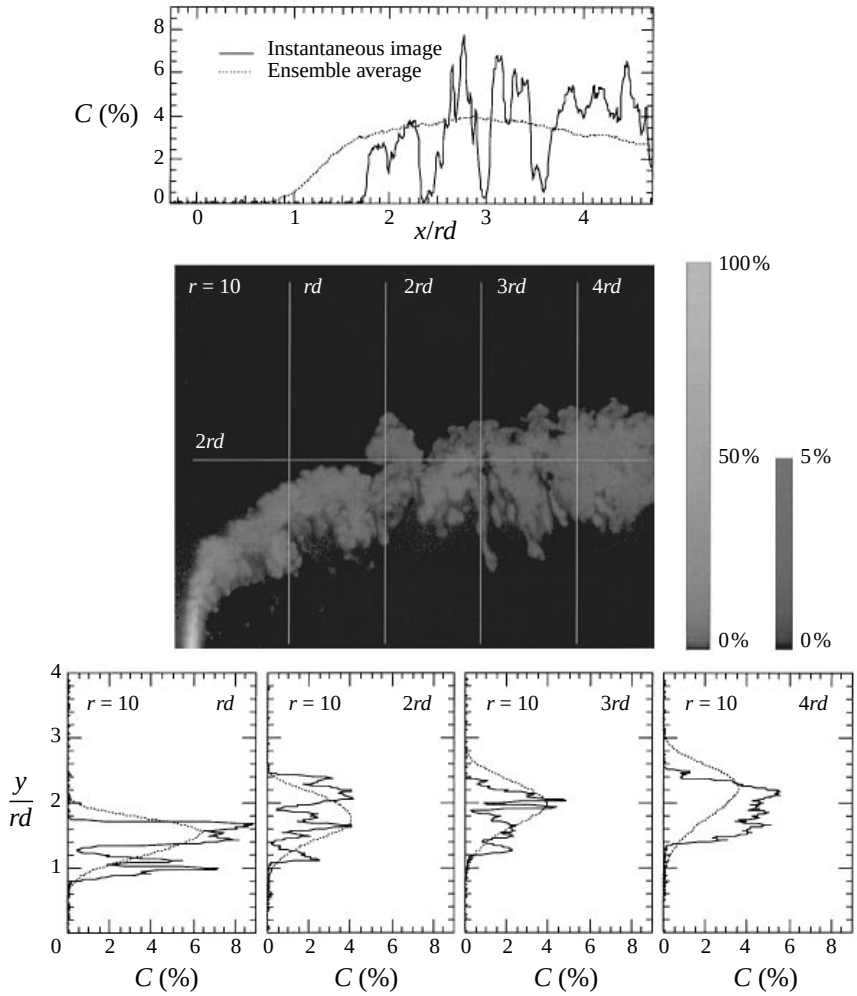


FIGURE 12. Instantaneous jet concentration field, side view, $r = 10$, $Re_j = 16\,600$.

result in a clearly defined edge between the presence of jet fluid and its absence. A fixed probe placed along the upper edge of the jet would find fluctuating periods between 0% (no jet fluid) and a finite value (jet fluid present).

In side-view images, other vortical structures are visualized as well. The jet shear layer is shown, but resolution is not adequate in the vortex interaction region for a clear presentation. The horseshoe vortex system is never seen because the crossflow boundary layer is not seeded in this experiment. Likewise in this $r = 10$ jet, the wake structures are not seen because no jet fluid is present in them. This image shows an instantaneous slice through the centre of the CVP.

End-view images clearly show the CVP. Figure 13 displays an $r = 10$ jet at $x = 2\,rd$. In this image, the CVP is tilted to the left. The peak concentration is in the upper side of the right-hand CVP lobe (see the vertical profile), which is in contrast to the higher concentration of the left lobe seen in the ensemble average. Multiple images (Smith 1996) show that the CVP is most often asymmetric, with one lobe typically maintaining a 5% to 15% greater concentration than the other; that value can rise

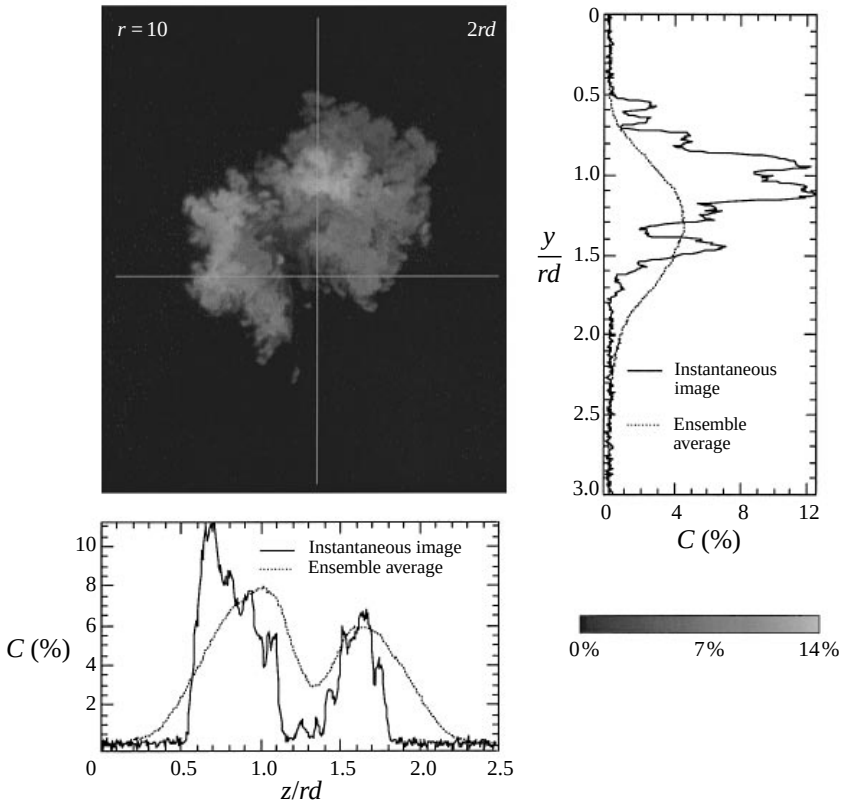


FIGURE 13. Instantaneous jet concentration field, end view, $x = 2\,rd$, $r = 10$, $Re_j = 33\,000$. Plots correspond to lines shown on the image.

to as high as 50% in individual images. Instantaneously, the dominant lobe can be either the right- or left-hand vortex of the CVP.

Figure 14 displays a plan-view image of the $r = 10$ jet at $y = 2\,rd$. On the left-hand side of this image, the jet is passing into the image plane, and on the right-hand side, the image plane is near the centre of the jet. Figure 14 shows that the free-stream penetrations along the upper edge of the jet occur as uniform streaks along the $z$-axis, giving the jet an axisymmetric mode as it progresses downstream. Sinusoidal variation is also observed (Smith 1996). The concentration profiles shown are chosen to highlight the axisymmetric nature, showing the positions where the jet fluid occurs. Again, note the sharp rises in concentration followed by small plateaus of similar concentration.

The $r = 20$ jet has a qualitatively similar instantaneous structure to the $r = 10$ jet, but it has specific features that are unique. To facilitate a complete comparison, three instantaneous images of the $r = 20$ jet are shown to complement the three $r = 10$ images shown in figures 12–14. Figure 15 shows an instantaneous side view of the jet concentration, figure 16 an end view and figure 17 a plan view.

The most striking difference between the $r = 10$ and $r = 20$ jet is the presence of jet fluid in the wake structures. Section 5 will provide a more detailed analysis, including a proposed mechanism for its appearance. In this section, only its physical features will be characterized. The jet fluid enters the wake in the form of thin fingers of fluid that can contain as high as 0.5% concentration jet fluid. These fingers remain

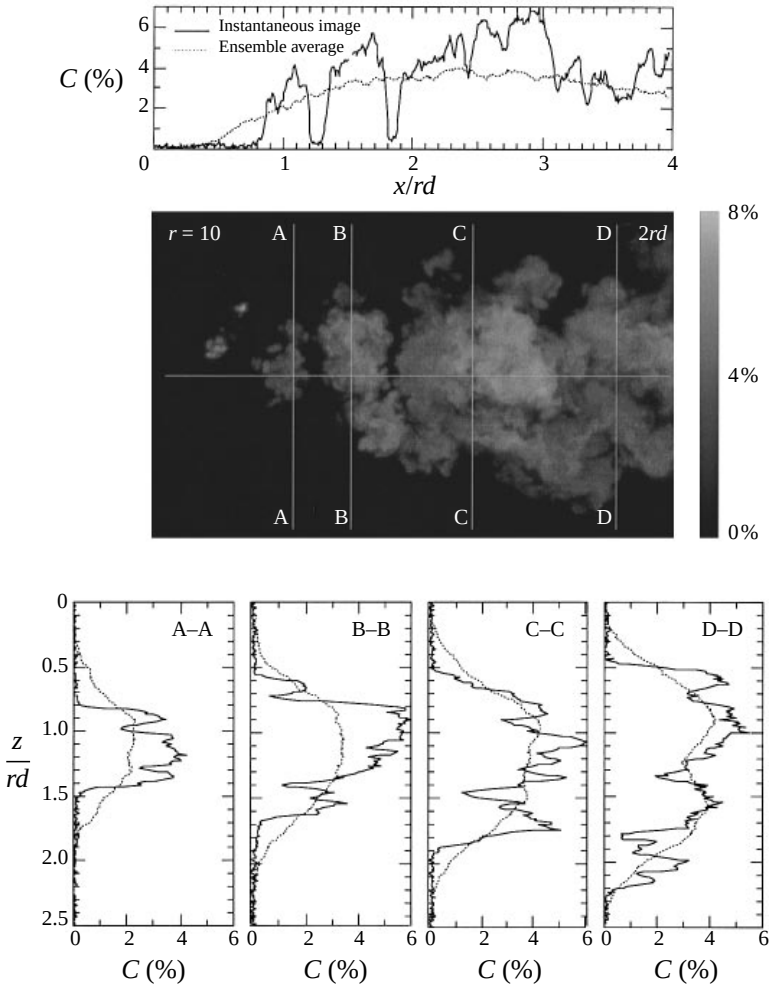


FIGURE 14. Instantaneous jet concentration field, plan view, $y = 2\,rd$, $r = 10$, $Re_j = 16\,600$.

primarily along the centreline of the jet as can be seen in figures 15 and 16; they connect to the jet body, but not to the tunnel wall. The connection to the jet body can occur to either CVP lobe, or to the jet centre, but if it connects to a CVP lobe, it is always connected to the weaker lobe (Smith 1996); connection to the right-hand CVP lobe is shown in figure 16.

The variations along the upper edge of the $r = 20$ jet, figure 15, are greater than those in the $r = 10$ jet. Penetration along the upper edge can occur past the jet centerline as large rolling structures form. The end-view image, figure 16, also shows the presence of the rollers along the upper edge of the jet, displaying out-of-plane motion in the upper left portion of the image.

Like the $r = 10$ case, the CVP shown in figure 16 is asymmetric with the peak values occurring in the left-hand lobe. Typical images show a peak concentration difference of 5% to 15% between the left- and right-hand lobes with peak values ranging as high as 50%. In the $r = 20$ jet the lower-concentration lobe always lies below the higher-concentration lobe, and the higher-concentration lobe may be larger in size as well.

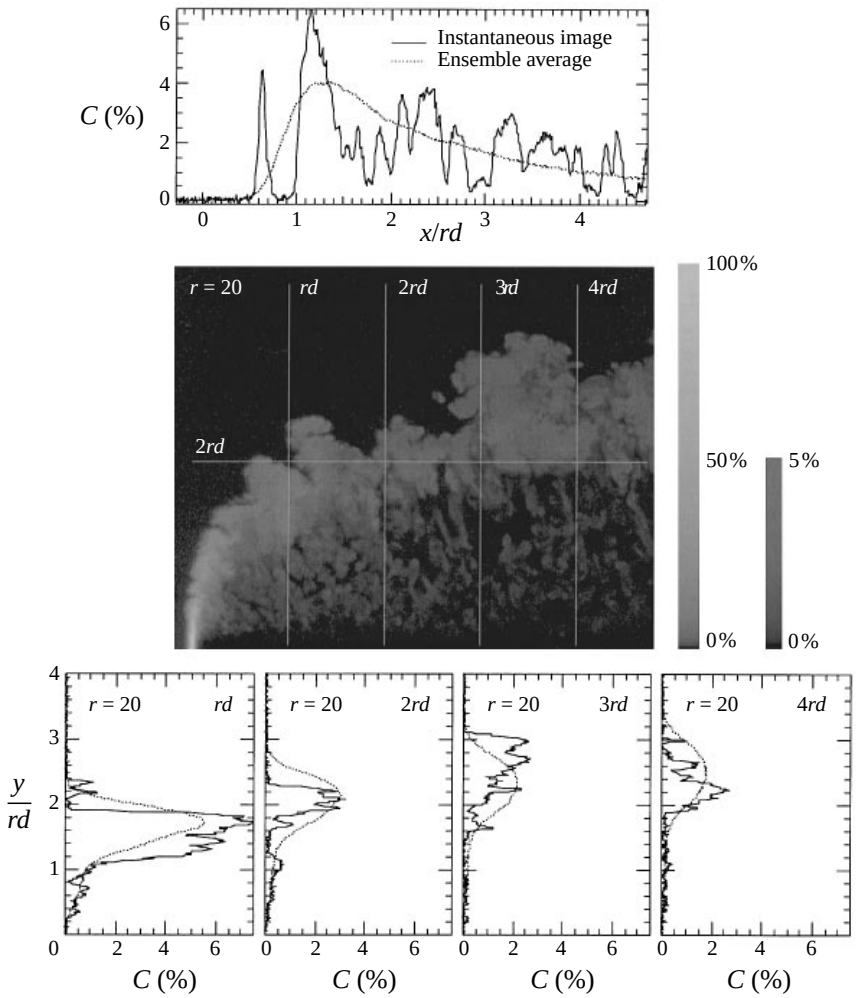


FIGURE 15. Instantaneous jet concentration field, side view, $r = 20, Re_j = 16\,600$.

Since the penetration of the $r = 20$ jet is slightly greater than the $r = 10$ jet, figure 7, the plan-view image at $y = 2\,rd$, figure 17, cuts slightly lower through the CVP than the $r = 10$ image. This image shows the dominant CVP lobe switching from side to side. It switches from the lower edge of the image to the top between lines B-B and C-C, and then from the top edge to the bottom between lines C-C and D-D. Quantitative statistics of the time the CVP remains dominant in a single lobe are not possible from these images due to a lack of instantaneous velocity data, but figure 17 gives a qualitative sense of the switching characteristics.

## 5. Jet fluid in the wake structures

Jet fluid has been shown to be present in the wake structures in an $r = 20$ jet, but not an $r = 10$ jet. Jet fluid in the wake structures has been previously reported by Lozano *et al.* (1993), and can be seen in the images of Shen (1991) for a vectored rectangular jet. Fric & Roshko saw no jet fluid in the wake structures up to $r = 10$. In

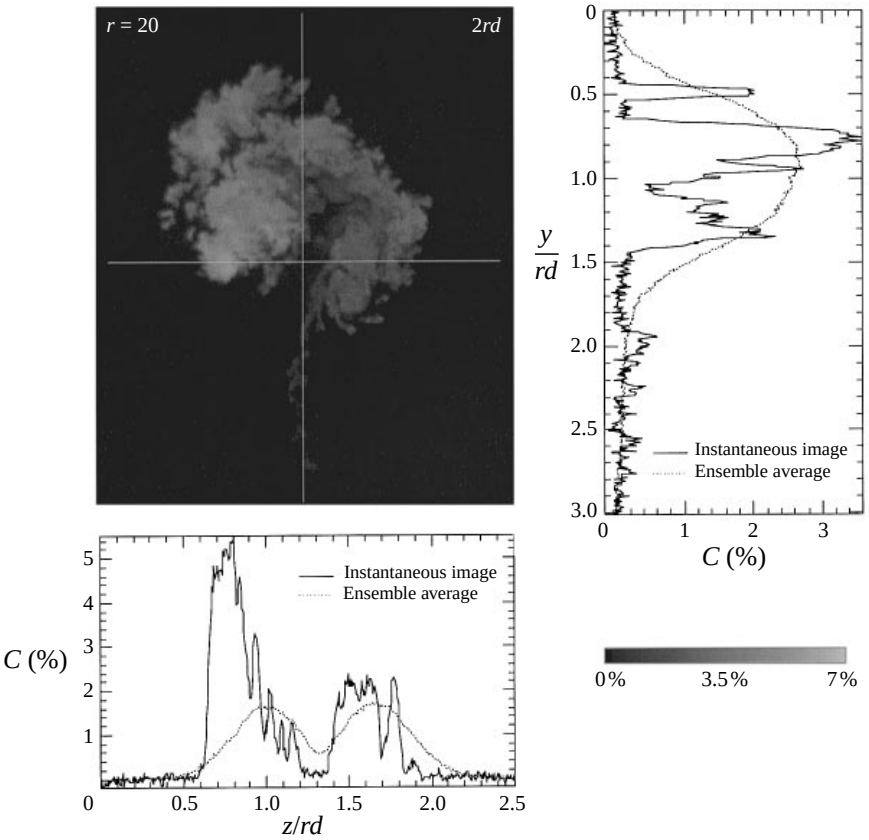


FIGURE 16. Instantaneous jet concentration field, end view, $x = 2rd$, $r = 20$, $Re_j = 33\,000$. Plots correspond to lines shown on the image.

this section a mechanism for the presence of jet fluid in the wake is proposed, based upon the analysis of Fric & Roshko (1994).

The transition from no jet fluid in the wake to its presence occurs from $r = 10$ to $r = 15$. Figure 18 shows instantaneous images at each of the six velocity ratios from 10 to 15. In these images, jet fluid is seen to penetrate the wake structures to an increasing depth with increasing velocity ratio. The $r$ values at which jet fluid penetration occurs are insensitive to Reynolds number over a factor of four (8400 to 33 000), and also insensitive to the relative ratios of the crossflow boundary layer thickness, the jet exit boundary layer thickness, and the jet exit diameter.

Fric & Roshko (1994) identify crossflow boundary layer vorticity as the origin of the vorticity in the wake structures, using a mechanism summarized in figure 19. Figures 19(*a*) and 19(*b*) are simultaneous side- and plan-view photographs of smoke wires seeding the crossflow boundary layer of an $r = 4$ jet (figure 28 from Fric & Roshko 1994). Figure 19(*c*), an $r = 5$ jet, is the best available match to this case from the PLIF data set. The Fric & Roshko images complement the PLIF image because they seed the crossflow boundary layer, and the PLIF image seeds the jet fluid. The label *b-1* shows the crossflow boundary layer separation, and *b-2* shows the same vortex after it has become attached to the lee side of the jet and turned up, becoming the wake structures. Fric & Roshko refer to structure *b-2* as the footprint of the wake

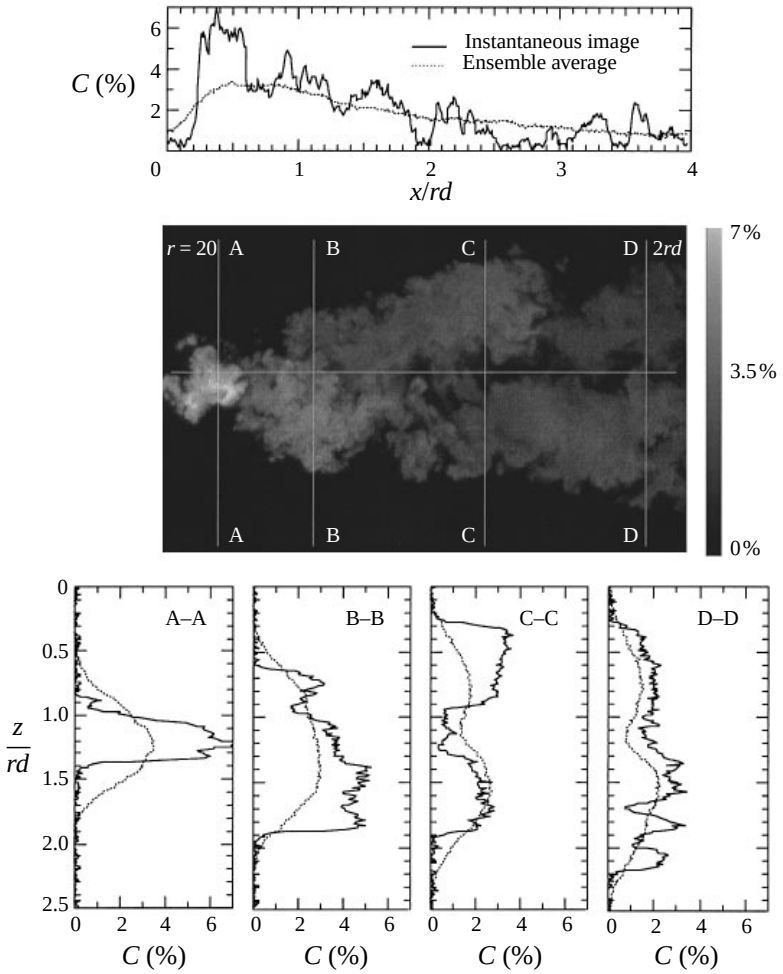


FIGURE 17. Instantaneous jet concentration field, plan view, $y = 2\,rd$, $r = 20$, $Re_j = 16\,600$.

vortex. Label *a-3* marks dense smoke, showing a bursting event (their terminology), where crossflow boundary layer fluid is pulled upward into the wake structures.

The three events, *1* the boundary layer separation, *2* the emergence of the wake vortex footprint, and *3* the bursting event, are labelled in each image, (*a*), (*b*) and (*c*) of figure 19, creating nine markers which show each event in each image. The assertion that the wake vorticity has its origin in the vorticity of the crossflow boundary layer is supported by Coelho & Hunt (1989) who conclude that little jet vorticity diffuses into the wake region.

Figure 19(*c*) suggests that Fric & Roshko may have overestimated the penetration of the bottom edge of the $r = 4$ jet (see figure 13*c* in Fric & Roshko 1994). They assume that the bursting event occurs below the jet body, but it is clear that the burst occurs into the jet path rather than along the jet bottom edge when comparing *a-3* and *c-3*.

Axial flow from a wall boundary condition through a vortex core has been established experimentally by Cohn & Koochesfahani (1993). It is suggested here that the bursting event in the $r = 5$ jet is caused when the CVP pulls the wake vortex into

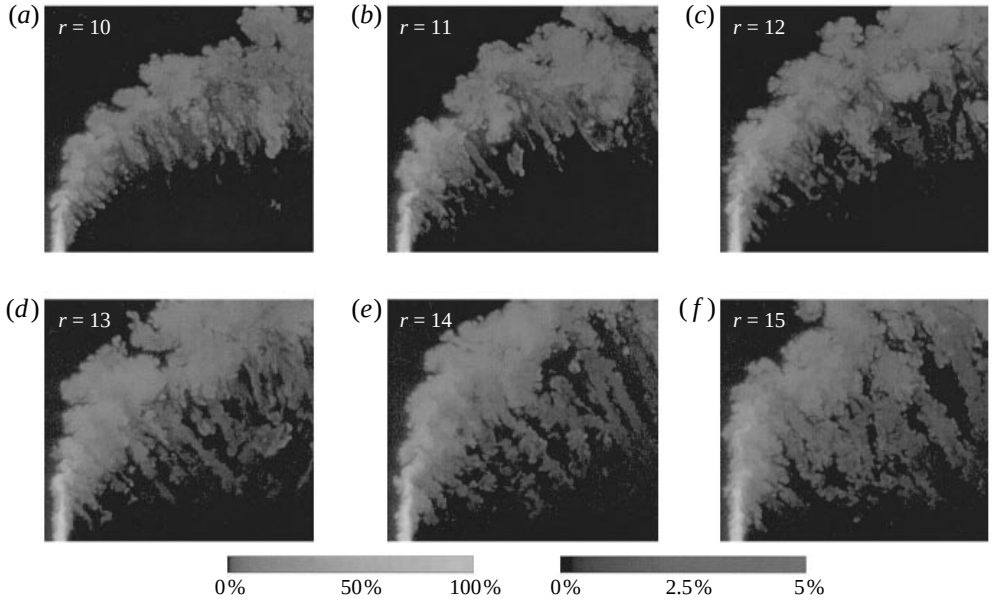


FIGURE 18. Side-view images, $r = 10$ to $r = 15$, $25d$ by $22.5d$, $d = 10$ mm, $Re_{cf} = 3300$, based on $U_{cf}$ and $d$. (*a*) $r = 10$, (*b*) 11, (*c*) 12, (*d*) 13, (*e*) 14, (*f*) 15.

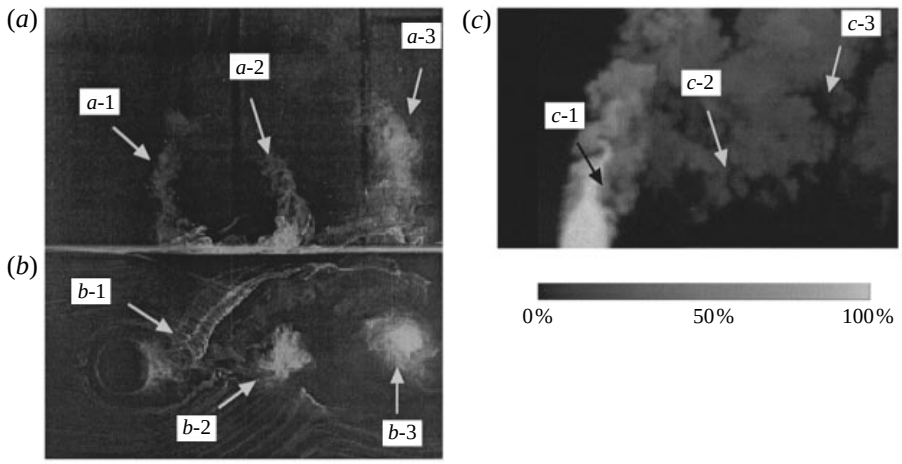


FIGURE 19. The Fric–Roshko roll-up mechanism, linking boundary layer vorticity to the vorticity in the wake structures: (*a*, *b*) simultaneous boundary-layer seeded smoke-wire photographs of an $r = 4$, $Re_j = 15\,200$ jet, (*a*) side view (*b*) plan view. The best view available matching case PLIF image (*c*) is an $r = 5$, $Re_j = 16\,600$ jet.

the jet, stretching it, and increasing its rotational velocity. If one envisions a vortex ending on a wall, the axial velocity is of order $(\Delta p/\rho)^{1/2}$, where $\Delta p$ is the difference between the ambient pressure and the vortex core pressure. The rotational velocity is of order $(2\Delta p/\rho)^{1/2}$, suggesting that the axial velocity can be comparable to the rotational velocity, a condition common in bursting. Note that in this formulation, it is the stretching of the vortex that ultimately causes the bursting event.

An extension of the Fric–Roshko mechanism can account for the presence of jet fluid in the wake structures. Figure 20 displays an $r = 5$ jet and an $r = 20$ jet. The

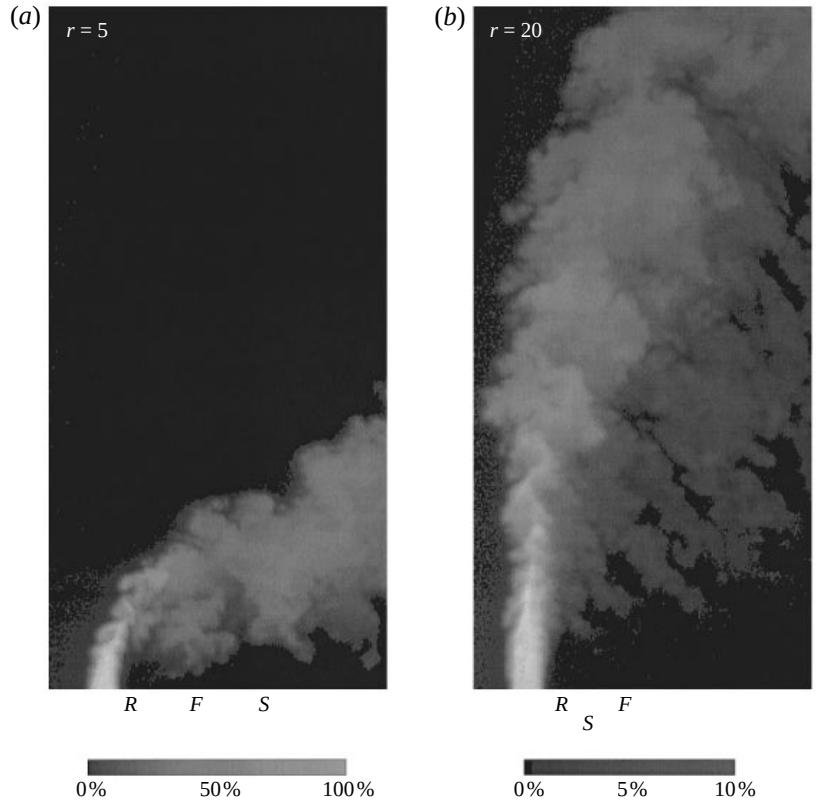


FIGURE 20. Instantaneous side-view images: (*a*) $r = 5$, $Re_j = 16\,600$; (*b*) $r = 20$, $Re_j = 33\,000$. In both cases $d = 10$ mm and image frame is $11d$ by $22d$.

labels *R*, *F* and *S* mark the proposed roll-up position (*R*), turned-up position where the wake footprint is visible (*F*), and vortex stretch position (*S*). *R*, *F* and *S* in figure 20 correspond to *1*, *2* and *3* in figure 19. In the $r = 5$ jet the three events occur in the order *R*, *F* then *S*, where the stretch is caused by the CVP. The trajectory of the $r = 20$ jet is so vastly different in physical space than the $r = 5$ case, that it is proposed that the vertical jet trajectory causes the vortex to stretch, before the wake footprint occurs. The order of events is now *R*, *S* and *F*. This has the effect of causing flow along the wake vortex axis from the jet fluid because the end of the vortex not connected to the jet is still in the form marked *b-1* in figure 19, and no flow from the wall occurs. The extension of the Fric–Roshko mechanism is based upon two points. First, Cohn & Koochesfahani (1993) also recorded axial flow along a vortex core from a wake boundary condition. Second, the images of Fric & Roshko show that the boundary layer vortex has turned up and shows a wake vortex footprint at approximately $d$–$2d$ downstream of the jet nozzle, regardless of the velocity ratio. Since the scaling of the vortex interaction region is based upon $d$, it is expected that the earliest footprint position of the crossflow boundary layer vorticity will continue to occur at $d$–$2d$ for $r > 10$.

The result of axial flow from the jet into the wake structures are shown as plan-view images in figure 21. The jet fluid downstream of the $r = 20$ jet marks the vortex cores of the wake structures. The $r = 10$ case shows no persistent jet fluid in the wake, even though wake structure vortex cores are present. Figure 21(*a*) is reminiscent of the von

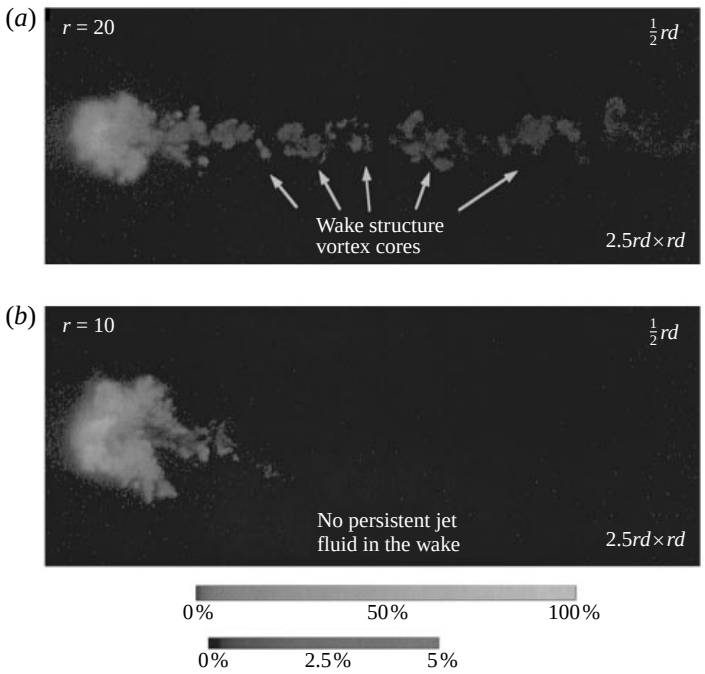


FIGURE 21. Instantaneous plan-view images comparing (*a*) the $r = 20$ jet, $Re_j = 33\,000$ and (*b*) $r = 10$ jet, $Re_j = 33\,000$.

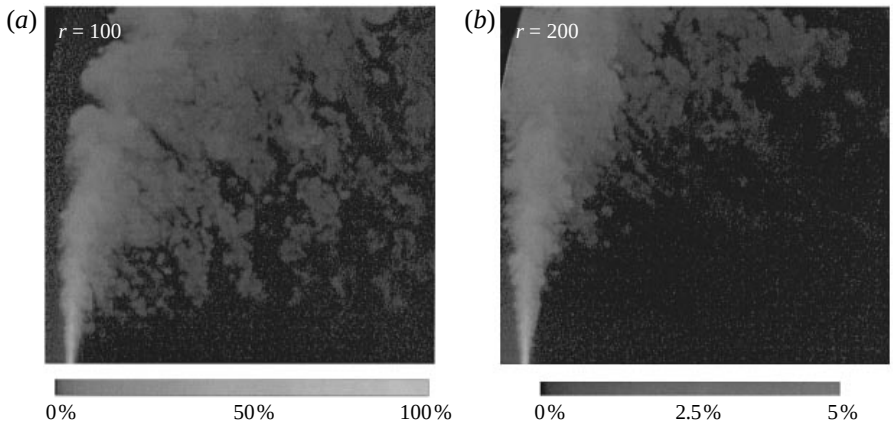


FIGURE 22. Instantaneous jet concentration images at high velocity ratios, (*a*) $r = 100$ (*b*) $r = 200$. In both cases $d = 2.0$ mm, images are 125 $d$ by 115 $d$, $U_{cf} = 1$ m s$^{-1}$.

Kármán vortex street for flow over a cylinder, but the mechanisms which create the wake structures are entirely different, as discussed by Fric & Roshko (1994).

This analysis of the vortex interaction region is based upon the local jet diameter, $d$. This scaling is the same as that of a free jet, but that should not imply that the region closest to the jet exit in a transverse jet in the range $r = 5$ to $r = 25$ will scale as a free jet. There is no direct analogy between the plan-view images of figure 21, and the corresponding free jet images shown by Liepmann & Gharib (1992), and the

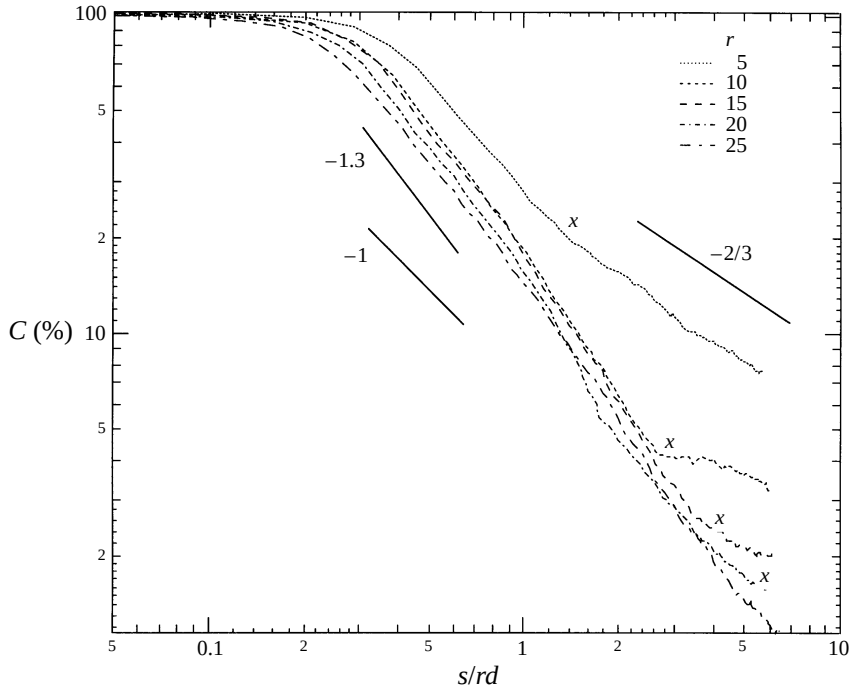


FIGURE 23. Maximum centreline concentration decay plotted with downstream distance $s$, normalized by $rd$.

next section will show that the transverse jet concentration never scales as $s^{-1}$ for $r < 25$ as the free jet does.

It is interesting to ask if an ever decreasing crossflow velocity would cause a region of the transverse jet to behave as a free jet. Figure 22 shows an $r = 100$ jet and an $r = 200$ jet. The $r = 200$ case shows that the jet fluid that enters the wake has lifted far away from the wall (about $60d$), raising the possibility that the $r = 200$ transverse jet may have free jet characteristics in the region below the wake structures.

## 6. Maximum centreline concentration decay

Each point of the trajectory data given in § 4 has associated with it a value of jet fluid concentration. These values, plotted against the downstream coordinate, $x$, or the jet centreline coordinate, $s$, show the maximum centreline concentration decay.

### 6.1. *Centreline decay, rd*

Figure 23 displays the centreline concentration decay along the centreline coordinate $s$ for $r = 5$ to $r = 25$. The $r = 15$, $r = 20$ and $r = 25$ lines connect data taken for each of the two $d$-cases shown in table 1 (i.e. two different jet diameters). The connection occurs at $s \approx rd$, and is necessary because the relative size of the smaller nozzles and the relative thickness of the laser sheet causes the maximum concentration values to be underpredicted near the jet exit. Figure 23 is shown as a log-log plot, so a power-law decay appears as a straight line. A decay of $s^{-2/3}$ is the far-field rate predicted in modelling efforts by Broadwell & Breidenthal (1984) and Hasselbrink *et al.* (1997) (both predictions are in $x$, but $s \sim x$ in the far field). Decay rates of $s^{-1.3}$ (best available near-field fit) and $s^{-1}$ (free jet decay rate) are also shown.

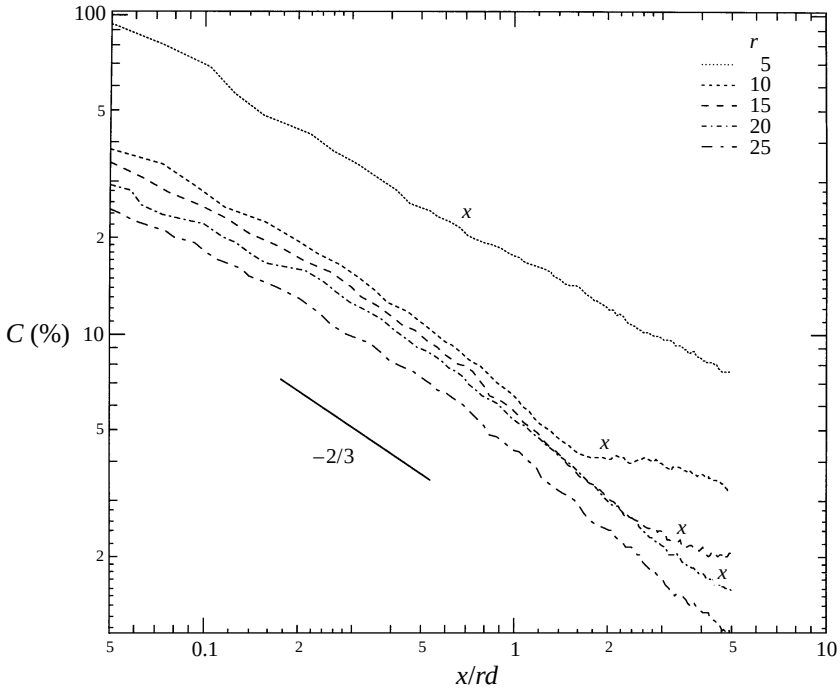


FIGURE 24. Maximum centreline concentration decay plotted with downstream distance $x$, normalized by $rd$.

For each jet, the centreline concentration remains 100% through the potential core, then decays initially at $s^{-1.3}$, an increase over the decay rate of a free jet, $s^{-1}$. During the shared $-1.3$ decay, the $r = 10$ to $r = 25$ jets nearly lie upon the same line when $s$ is normalized with $rd$. At $s/rd$ locations specific to each value of $r$, the centreline decay branches away from the $-1.3$ decay rate. Much interest in the transverse jet results from its enhanced mixing properties, making the regions before and just after the branch points important areas of study. These branch points are labelled $x$. The $r = 25$ jet is not deemed to have reached a branch point yet, and the different path of the $r = 5$ jet is consistent with it belonging to a different class of transverse jets.

The branch points are also present if the decay is shown against $x/rd$, plotted in figure 24. The $x^{-2/3}$ decay is displayed for comparison. The branch points occur at $x = 0.8\,rd$ for the $r = 5$ jet, at $x = 2\,rd$ for $r = 10$, $x = 3\,rd$ for $r = 15$ and $x = 4\,rd$ for $r = 20$.

The position of the branch points is insensitive to changes in the jet exit Reynolds number over a factor of four (8400 to 33 000) as seen in figure 25 for the $r = 10$ jet.

A scaling analysis using $rd$ normalization will highlight the role of the branch points. Following Hasselbrink & Mungal (1996), consider only the jet fluid in a uniform-density transverse jet flow field. The volume flux of jet fluid out of the nozzle must equal that through an arbitrary plane $x$ = constant well into the far field as shown in figure 26. $Q_{in} = U_j A_j$, assuming a uniform jet exit velocity, $U_j$, and area, $A_j$, and

$$Q_{out} = \int_A C\, \boldsymbol{V}_j \cdot \mathrm{d}\boldsymbol{A},$$

where $C$ is the jet concentration, and $\boldsymbol{V}_j$ the local velocity vector.

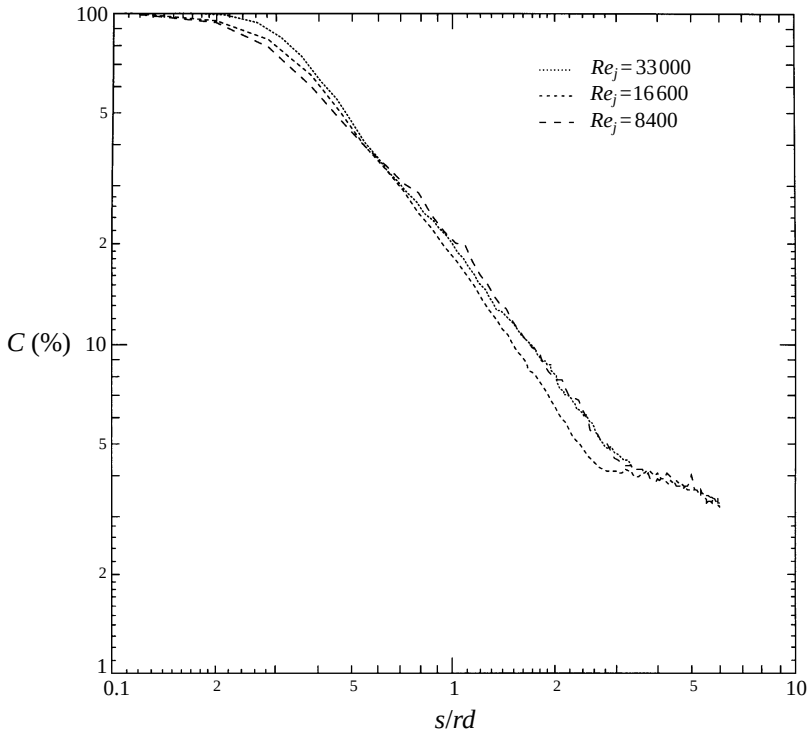


FIGURE 25. Centreline concentration decay of the $r = 10$ jet over a factor of four change in jet exit Reynolds number.

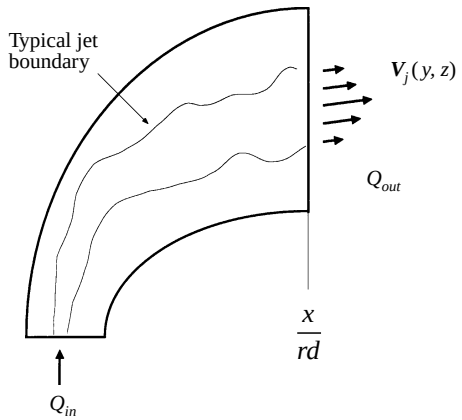


FIGURE 26. Integral, control-volume approach to conservation of jet fluid.

Setting $Q_{in} = Q_{out}$ gives

$$\frac{\pi}{4}\,\frac{(rd)^2}{r} = C_m \int_A \frac{C}{C_m}\,\frac{\boldsymbol{V}_j}{U_{cf}} \cdot \mathrm{d}\boldsymbol{A}, \tag{6.1}$$

where $C_m$ is the maximum local centreline ($z = 0$) concentration. In this experiment $rd$ is held constant, and if $\int_A C/C_m\, \boldsymbol{V}_j/U_{cf} \cdot \mathrm{d}\boldsymbol{A}$ is a constant (to be discussed with

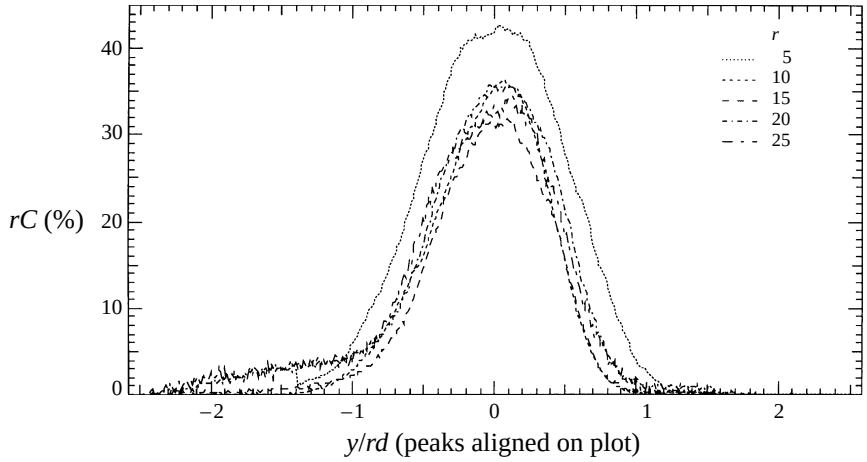


FIGURE 27. Scaled ($rC$) centreline concentration profiles, $x = 4\,rd$, $z = 0\,rd$, $Re_j = 16\,6000$ in all cases.

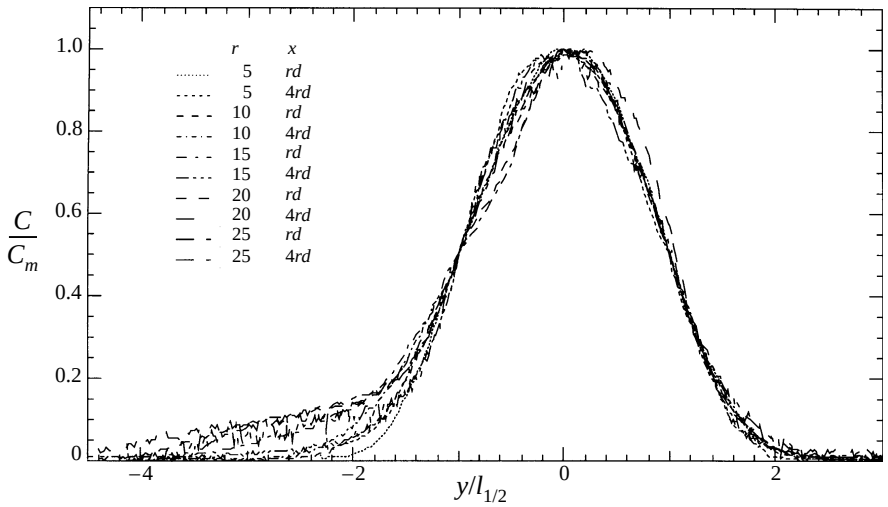


FIGURE 28. Vertical centreline profiles at $x = rd$ and $x = 4\,rd$: $C$ normalized by local maximum $C_m$, $y$ normalized by half-width at half maximum, $l_{1/2}$.

self-similarity in § 6.2), then in the jet far field,

$$C_m \sim \frac{1}{r} \tag{6.2}$$

or $r\,C_m$ is a constant for a specific $x/rd$ location downstream for a range of $r$. Physically, the scaling is a result of decreasing $d$ while increasing $r$ causing $Q_{in} \sim rd^2 \sim 1/r$ for $rd$ a constant.

Figure 27 shows the concentration profiles at $x = 4\,rd$ for $r = 5$ to $r = 25$. The vertical axis is now $r\,C$ and the near-uniform values of $r\,C_m \approx 33\%$ (the $r = 5$ jet deviates from this value) show $C_m \sim 1/r$ scaling is obtained after the branch points. Thus the role of the branch points is to transition the flow field from an $s^{-1.3}$ decay, occurring along the same decay line, to a decay rate of $s^{-2/3}$, recovering a $C_m \sim 1/r$ relationship.

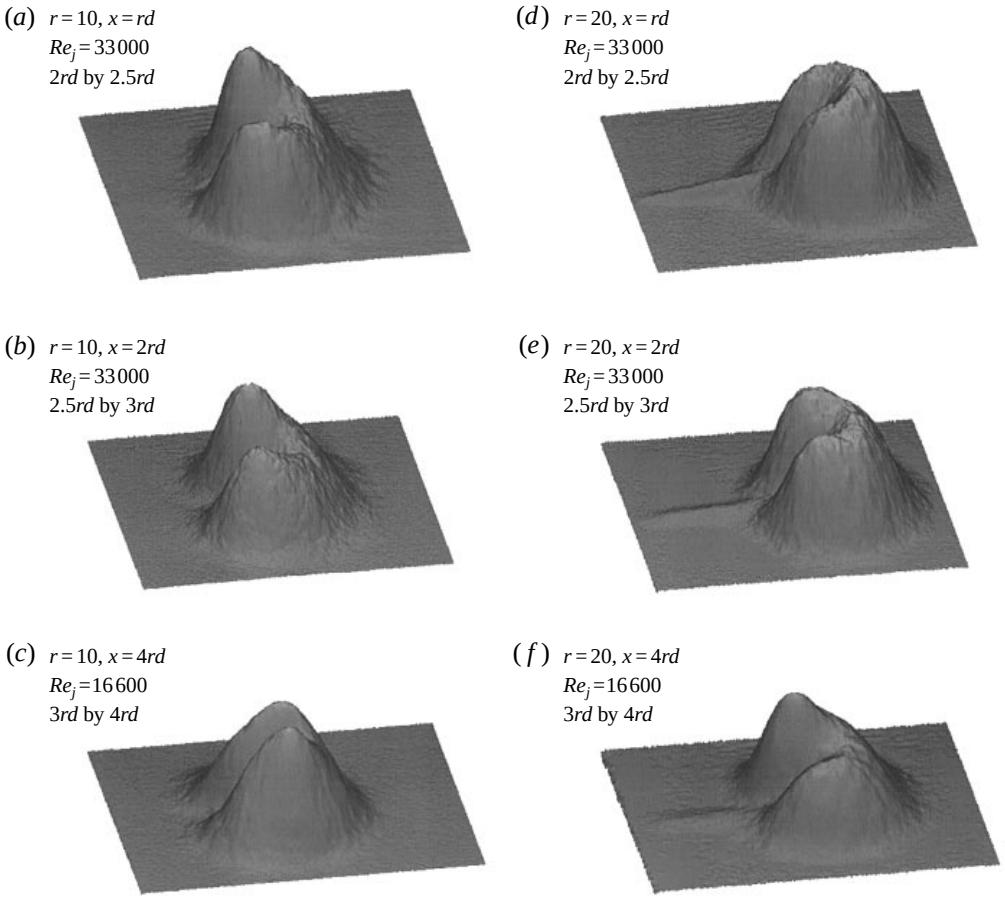


FIGURE 29. Three-dimensional end-view ensemble averages. The height of these images is raised linearly in proportion to the jet concentration.

Structurally, the branch point positions correspond with the downstream development of the CVP. The CVP development in the $r = 20$ jet occurs at $s/rd$ locations farther downstream than the $r = 10$ jet. The branch points maintain the same relationship, $r = 10$ at branch point $x = 2\,rd$ and $r = 20$ at branch point $x = 4\,rd$. Other features of the branch points will be discussed through the remainder of this paper.

### 6.2. *Self-similarity*

In its most simple description, a self-similar flow has average velocity, scalar concentration and turbulence statistics that can be collapsed by a single spatial variable. The concentration profiles in the $z = 0$ plane do collapse when normalized by their local maximum value, $C_m$, and the half-width at half-maximum, $l_{1/2}$, shown in figure 28 for data before the branch points ($x = rd$) and after ($x = 4\,rd$). The wake structure causes the deviation between $y/l_{1/2} = -4$ and $-2$.

Complete self-similarity requires the $(y, z)$-plane to collapse to similar profiles. The ensemble-averaged end-view data are shown again in figure 29 this time as three-dimensional images, where the height is raised linearly in proportion to the jet

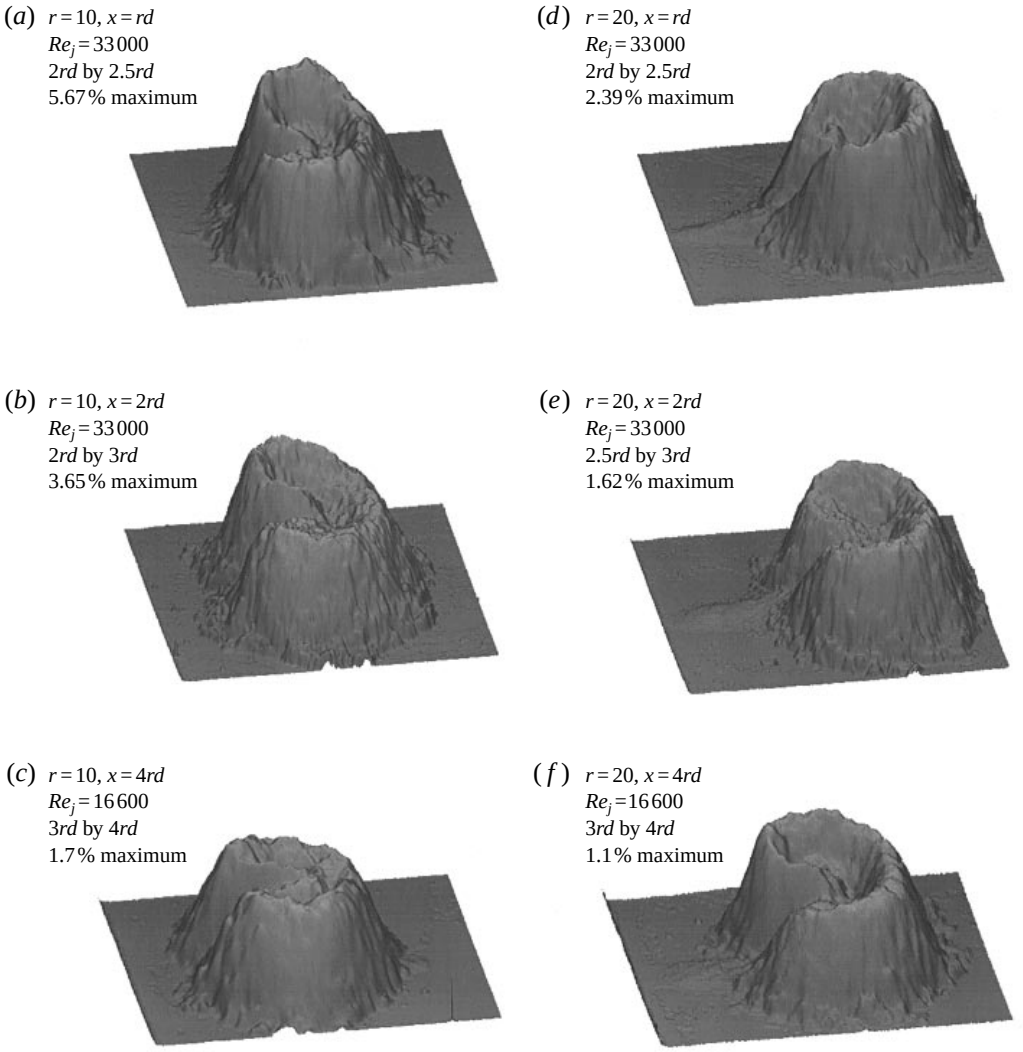


FIGURE 30. Three-dimensional r.m.s. images. The height of these images is raised linearly in proportion to the r.m.s. value.

concentration. These images clearly display different profiles. There is no similarity among the same $r$ at different $x$ (compare $a, b$ and $c$ together and compare $d, e$ and $f$ together) and there is no similarity between the same $x$ at different $r$ (compare $a$ with $d$, $b$ with $e$, and $c$ with $f$). From the end-view profiles it is established that full self-similarity does not occur in the jet in crossflow for $x < 5\,rd$ using $rd$ normalization. Figure 30 displays three-dimensional images of the r.m.s. end views, serving to confirm the lack of complete self-similarity.

In the scaling analysis that produced $C_m \sim 1/r$, it is assumed that the surface integral $\int_A C/C_m \, \boldsymbol{V}_j/U_{cf} \cdot \mathrm{d}\boldsymbol{A}$ is constant. This assumption relies upon the jet being self-similar, and the result that $r\,C_m \approx 33\%$ at $x = 4\,rd$ is shown to be accurate to $\pm 8\%$ in figure 27. Thus the assumption of self-similarity leads to reasonable results, despite the lack of complete self-similarity.

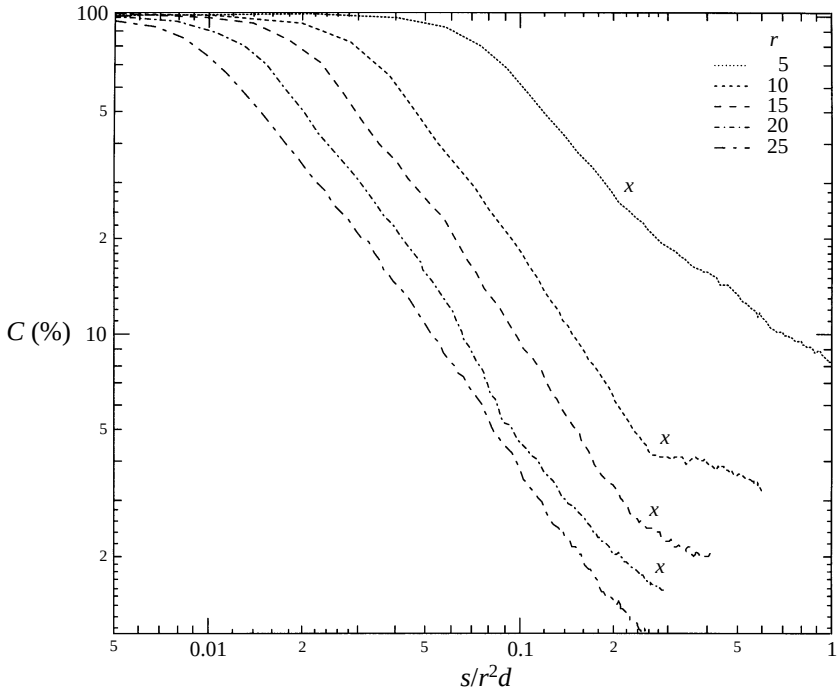


FIGURE 31. Maximum centreline concentration decay plotted with downstream distance $s$, normalized by $r^2d$.

### 6.3. *Centreline decay, $r^2d$*

The maximum centreline concentration decay plotted against $s/r^2d$ is shown in figure 31, and this scaling is seen to align the branch points at $s/r^2d = 0.3$, which corresponds to $x/r^2d \approx 0.2$. The position of the branch points at $x/r^2d \approx 0.2$ is the best use of normalizing by $r^2d$ and provides a convenient definition of the jet far field, $x/r^2d > 0.2$. Based upon the lack of self-similarity seen in the end views, the region $x/r^2d < 0.2$ is labelled the near field. The near-field label is due in part to the belief that effects from the $d$-scaled vortex interaction region still persist at $x/r^2d < 0.2$; a good example is the formation process of the CVP.

The end-view data of figure 29 suggest that self-similarity may occur beginning at the branch points. The possibility is raised by the similarity between the $r = 10$ jet at $x = 2rd$, (figures 29*b* and 30*b*) and $r = 20$ at $x = 4rd$ (figures 29*f* and 30*f*) notwithstanding the lack of symmetry and wake structures. Additional data would be necessary to determine if self-similarity occurs beginning from the branch point positions.

### 6.4. *Centreline decay, $d$*

Figure 32 displays the maximum centreline concentration decay plotted against $s/d$. The 100% concentration regions show that the potential core lengths, $l_{pc}$, increase with increasing $r$: $l_{pc} = 1.5d$ at $r = 5$ and $l_{pc} = 3d$ at $r = 25$. The differences in potential core length make the $r = 5$ jet the best mixer if the final desired maximum jet concentration is greater than 20%. Below 20% the branch points cause the decay lines to cross, which makes the choice for $r$ dependent upon the final desired concentration.

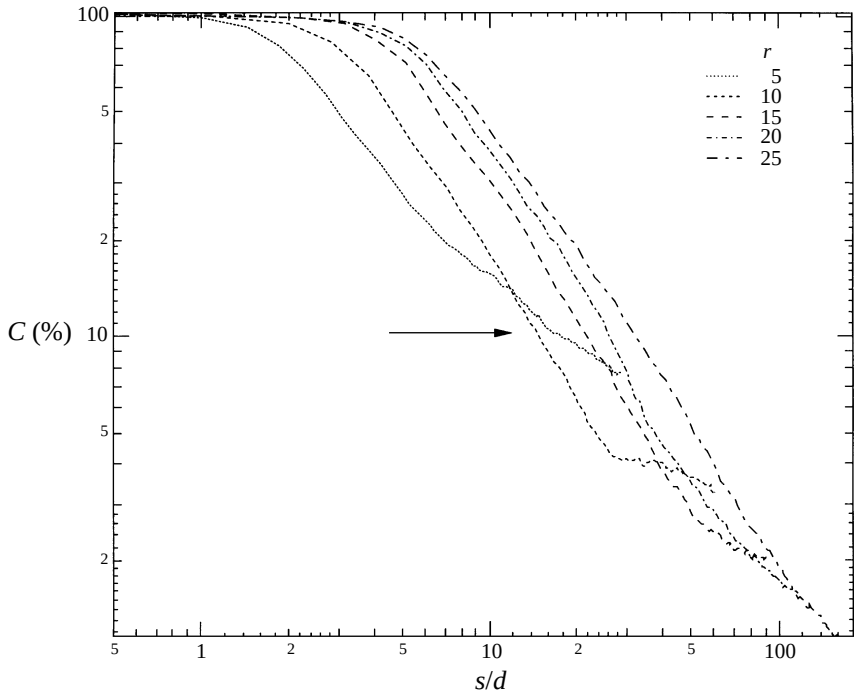


FIGURE 32. Maximum centreline concentration decay plotted with downstream distance $s$, normalized by $d$.

The crossing of the decay lines is postulated to be the physical mechanism behind the flame length minimum described in Broadwell & Breidenthal (1984). They discharge water jets containing an alkali, phenolphthalein, which colours the jet red, into an acidic liquid crossflow. When chemically mixed with $\phi$ parts by volume of crossflow fluid, the jet becomes colourless. They referred to the distance to colour disappearance as the flame length even though there is no heat release involved. Flame length data from Broadwell & Breidenthal are included in figure 33, which also includes flame length data of a propane flame from Brzustowski (1977). The flame length is plotted against $1/r$ so that $1/r = 0$ corresponds to free jet data. Figure 33($a$) shows that in both cold and combusting flows a minimum flame length is found at $r \approx 20$.

The physical mechanism which explains the minimum flame length is the crossing of the decay lines when $d$-scaled, figure 32. For example if a final concentration of 10% is required (see arrow in figure 32) the five $r$ cases each require a different chord length to reach the 10% point. An order-of-magnitude plot of these different lengths is presented as figure 33($b$), and the minimum flame length has been recreated. Furthermore, it is clear from figure 32 that the minimum flame length will vary with stoichiometry.

Note, the centreline decay rates show that the branch points are the physical mechanism behind the minimum flame length. The true local maximum value as seen in end-view data is often off the $z = 0$ plane. Therefore figure 32 will underpredict actual flame lengths and is not recommended for that use, especially taking into account jet asymmetry.

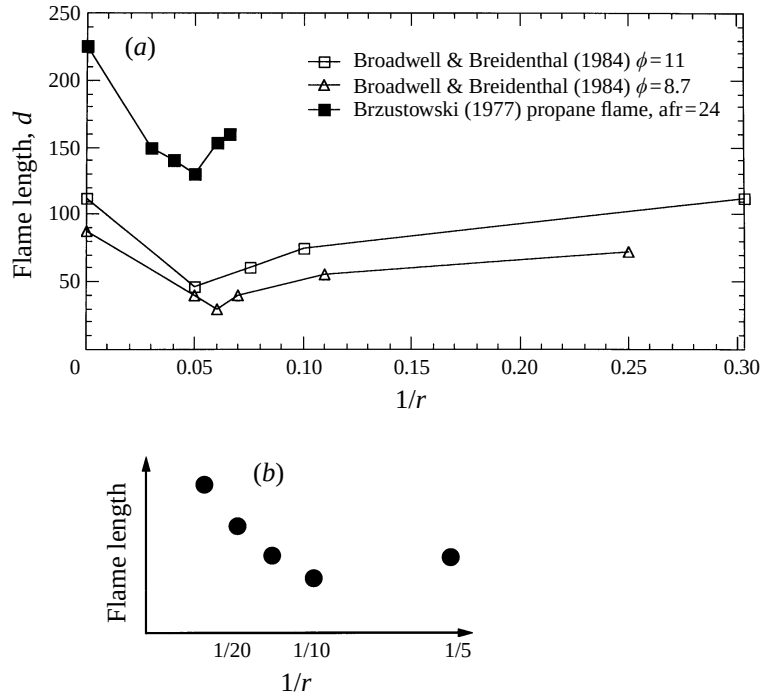


FIGURE 33. Measured flame lengths of the transverse jet. (*a*) Liquid data from Broadwell & Breidenthal (1984), $\phi$ is volume of ambient fluid (seeded with acid) required to turn jet fluid (seeded with coloured base) clear. A propane flame (air to fuel ratio of 24) has the same minimum. (*b*) Sketch of flame length for current centreline data, mixed to 9 parts ambient fluid for each part jet fluid (a concentration of 10%).

## 7. Probability density functions of mixture fraction

The probability density function (p.d.f.) of mixture fraction, $\xi$, is calculated at a point by forming histograms of the instantaneous pixel values, giving

$$p(\xi)\,\mathrm{d}\xi = \text{Probability}\{\xi - \tfrac{1}{2}\nabla\xi \leqslant \xi \leqslant \xi + \tfrac{1}{2}\nabla\xi\} \tag{7.1}$$

The p.d.f., $p$, is normalized such that,

$$\int_0^1 p(\xi)\,\mathrm{d}\xi = 1. \tag{7.2}$$

Recent liquid mixing layer results by Karasso & Mungal (1996) categorize p.d.f. results into three types: non-marching, marching and tilted, described in figure 34. The preferred value of concentration in a non-marching p.d.f. is invariant across the mixing region; the preferred value in a marching p.d.f. approaches the average layer concentration, merging smoothly with the delta function at zero concentration. A tilted p.d.f. slants toward the average profile, but the probability of the preferred concentration goes to zero before it merges at zero concentration. The results of Karasso & Mungal (1996) show that the fully developed two-dimensional, turbulent mixing layer evolves to a tilted p.d.f. A broader discussion of the p.d.f. and its implications for mixing can be found in Broadwell & Breidenthal (1982).

To obtain the volume of data points necessary to construct a p.d.f., it is necessary (Clemens & Mungal 1995; Karasso & Mungal 1996) to use multiple data points

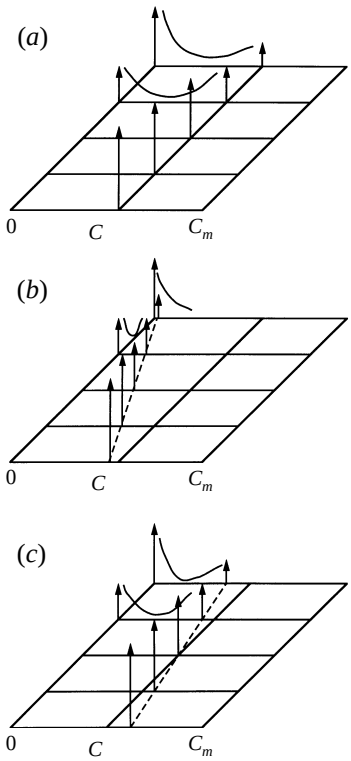


FIGURE 34. Idealized p.d.f.s: (*a*) non-marching type, (*b*) marching type, (*c*) tilted type.

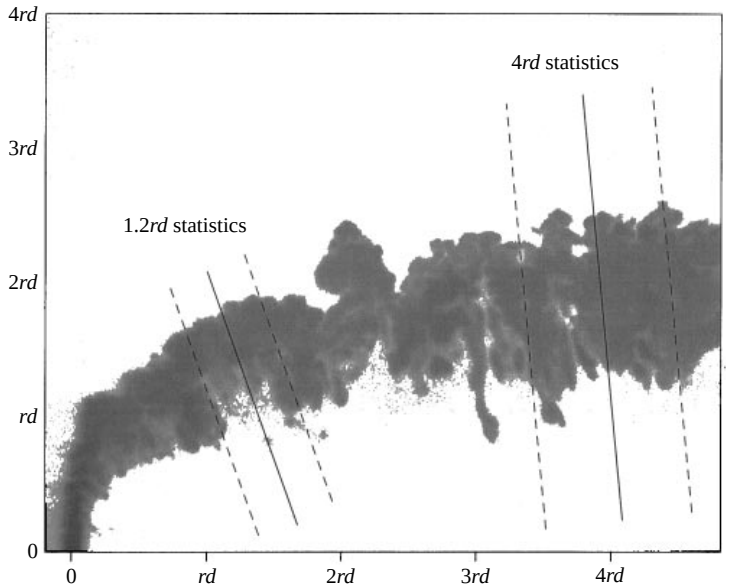


FIGURE 35. P.d.f. statistics acquired at positions marked. Nominal locations measured (solid lines) and actual range of columns used (dashed lines) are marked.

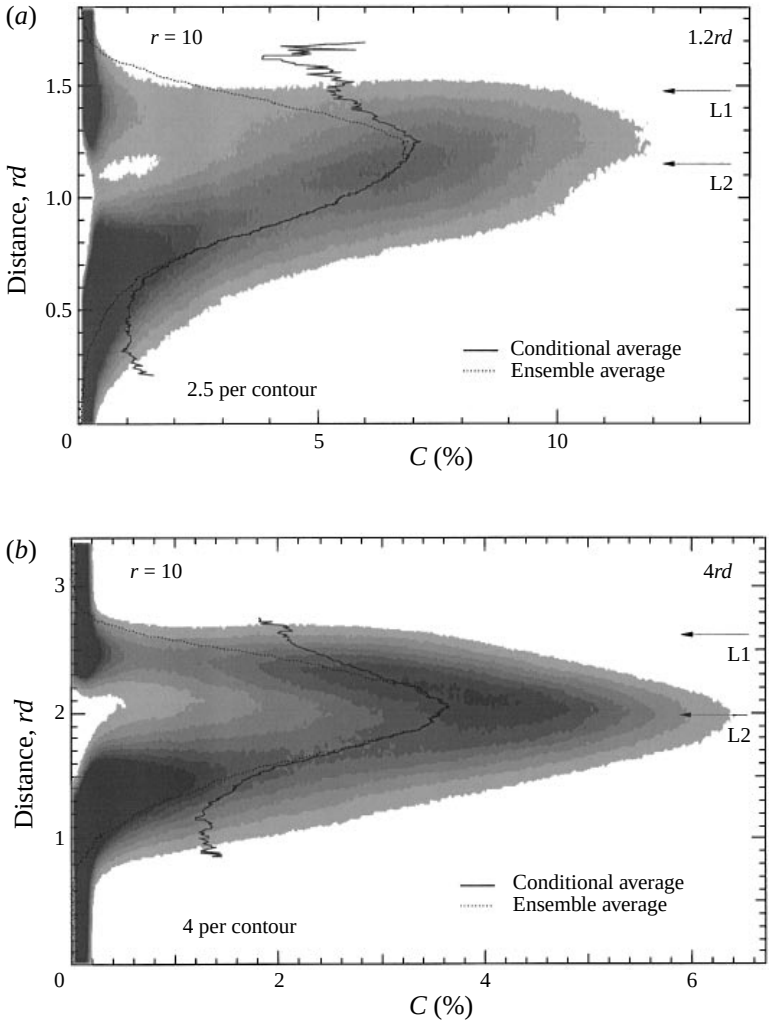


FIGURE 36. P.d.f. of mixture fraction: (*a*) $r = 10,\ x = 1.2\,rd,\ Re_j = 33\,000$, (*b*) $r = 10,\ x = 4.0\,rd,\ Re_j = 16\,600$.

from each PLIF image to represent a single point of the p.d.f. The complete p.d.f. consists of multiple single-point p.d.f. statistics acquired along a line of data called a column, even though it is not strictly vertical, as shown in figure 35. Histograms are constructed from one hundred columns of data, from each instantaneous image, marked by dashed lines resulting in the 100 points in each row creating the local single-point p.d.f. The nominal location of the p.d.f. measured is given by the solid line.

P.d.f. results for the $r = 10$ jet at $x = 1.2\,rd$ and $x = 4.0\,rd$ are shown in figure 36. The p.d.f. is shown as a contour plot: the vertical axis is the distance across the jet; the horizontal axis the concentration, $C$. The p.d.f. value, the probability of finding jet fluid at the specified concentration, is shown as contours. The ensemble-averaged values and conditional average (average when jet fluid is present greater than 0.25%) are also shown. The contour plots display the full structure of the p.d.f.

A more traditional display of the p.d.f. is shown in figure 37(*a*, *b*), which duplicates

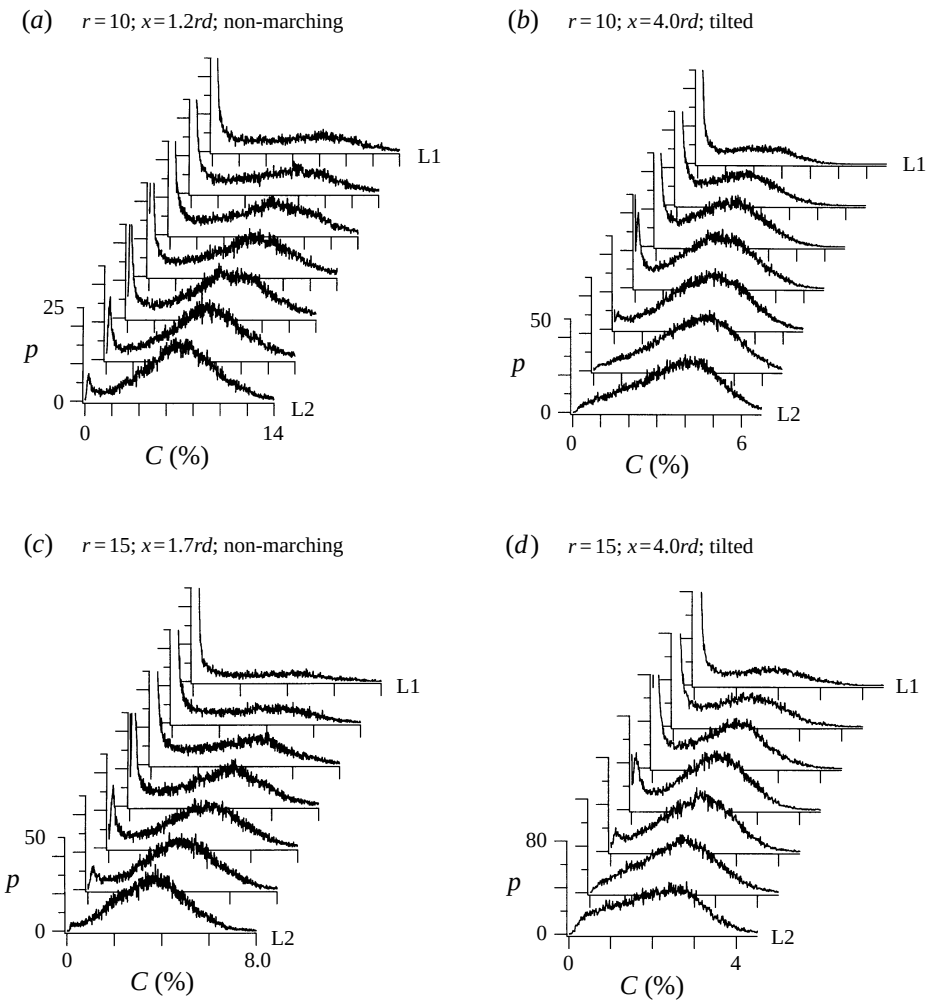


FIGURE 37 (*a–d*). For caption see facing page.

results from the contour plot of figure 36. Figures 37(*a*) and 37(*b*) show p.d.f. results along the upper edge of the jet corresponding to L1 and L2 in figure 36. From figure 37, it is possible to classify the p.d.f. as non-marching, marching, or tilted. In the case of the $r = 10$ jet, the p.d.f. is non-marching at $x = 1.2\,rd$ and tilted at $x = 4.0\,rd$. Thus the $r = 10$ jet has evolved to tilted after its branch point at $x = 2\,rd$. The pattern continues and the $r = 15$ jet evolves as well, shown in figures 37(*c*) and 37(*d*). The $r = 20$ jet remains non-marching up to $x = 4\,rd$, figure 37(*f*), and it is suspected that the transition to a tilted p.d.f. occurs just after the branch point. Figure 37(*g*) shows that the $r = 25$ jet is still non-marching at $x = 4\,rd$, and figure 37(*h*) shows that the $r = 5$ jet is also non-marching at $x = 4\,rd$. That the $r = 5$ jet does not transition after its branch point is consistent with it belonging to a different regime of transverse jets.

The p.d.f. results are consistent with the structural picture of the jet. The $r = 20$ jet is seen to have deeper upper-edge free-stream penetrations than the $r = 10$ jet. In the region considered, $x > 2\,rd$, the $r = 10$ jet had already transitioned to a tilted p.d.f., while the $r = 20$ jet was still in its non-marching, near-field region. A non-marching

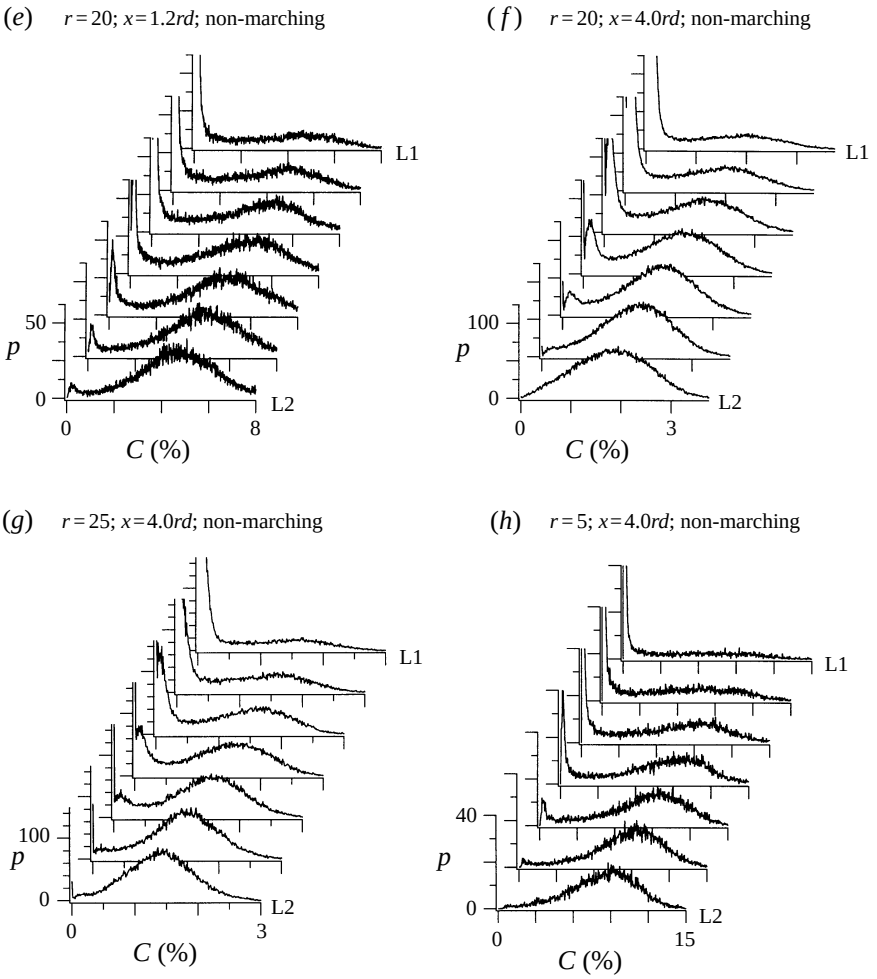


FIGURE 37. P.d.f. of mixture fraction, upper jet edge to centre. Each case is characterized as non-marching or tilted. Before the branch points, the p.d.f. is non-marching, and after it is tilted. The $r = 5$ jet is the lone exception.

p.d.f. has a preferred concentration of jet fluid that is invariant along the radial direction from which the p.d.f. is measured, regardless of distance from the centreline. That invariance would require large moving structures along the upper edge of the jet. Similarly, the tilted p.d.f. shows a preferred concentration that decreases as the p.d.f. is measured farther from the jet centreline, suggesting a change in the evolution of the mixing of the jet in crossflow.

## 8. Conclusions

The results from extensive imaging of the planar concentration field of the jet in crossflow are presented. Data are obtained using PLIF with acetone vapour, over a range of $r$ from 5 to 200, covering a range of jet exit Reynolds numbers from 8400 to 41 500. Instantaneous images of the transverse jet are characterized by sharp rises in concentration resulting in small, distributed regions of high-concentration fluid. The instantaneous images show deep penetration of free-stream fluid into the upper

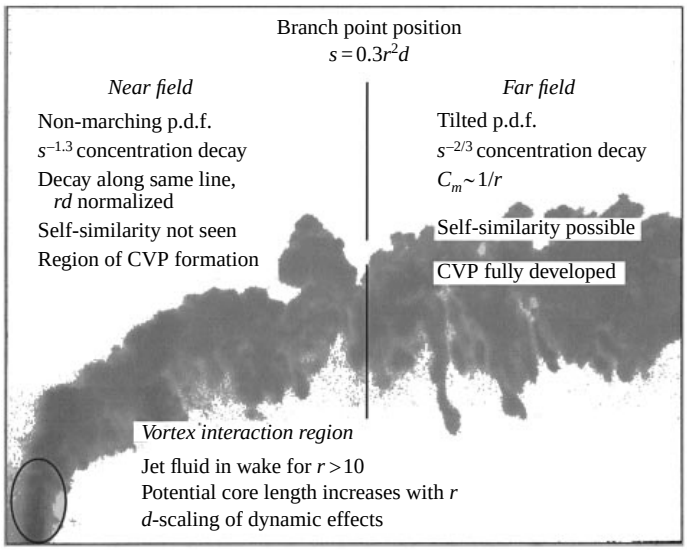


FIGURE 38. Features of the jet in crossflow for $r = 10$ to $r = 25$.

edge of the jet. They also show jet fluid penetrating the wake structures from $r = 10$ to $r = 15$, a feature which persists as high as $r = 200$. Ensemble-averaged images show that the formation of the CVP is delayed in higher-velocity-ratio jets, and that the jet concentration is asymmetric about the $z = 0$ plane. Maximum centreline concentration decay results show that the jet initially decays at a rate $s^{-1.3}$, and then adopts a slower rate, believed to reach $s^{-2/3}$ from modelling work. Quantifying the mixing across the upper edge of the $z = 0$ plane shows that the jet evolves from a non-marching to a tilted p.d.f. character.

These results are interpreted using three length scalings, $d$, $rd$, and $r^2d$. Results are summarized in figure 38. The vortex interaction region shows boundary layer separation and vortex roll-up events that scale on jet diameter. The $d$-scaling allows for structural effects that are dependent on $r$. These include the bursting events which peak at $r = 4$ seen by Fric & Roshko and the jet fluid in the wake structures which appear for $r > 10$. The $r$-dependent effects also include the delayed formation rate of the CVP in higher-velocity-ratio jets.

The trajectory and physical dimensions of the jet scale with $rd$. When the mean centreline concentration decay is plotted against $s/rd$, each jet has an initial decay proportional to $s^{-1.3}$, collapsing nearly upon the same line. Each jet then branches away, and together the jets recover a $1/r$ maximum concentration scaling. The branch points occur at a uniform position of $s/r^2d = 0.3$. The $r^2d$-scaling provides a convenient boundary between the region of decay rate $s^{-1.3}$, and the slower decay rate region. Self-similarity is not seen in the ensemble-averaged end views, although it is possible that self-similarity occurs after the branch point positions. The lack of self-similarity in the $s^{-1.3}$ region is the reason why it is labelled the near field in this work. The region $x/r^2d > 0.2$ is labelled the far field.

It should be noted that the near field is the region of CVP development, and the far field is the region where the CVP is fully developed. Thus the CVP itself does not enhance mixing compared to the free jet as the CVP is in the far-field ($s^{-2/3}$) region. Rather it is the structural formation of the CVP that corresponds to the enhanced mixing region, the near field.

Because of the changes in the transverse jet which occur at the branch points, the branch points are viewed as a transition region in the flow. This view is supported by the p.d.f. results, which show a non-marching character before the branch points, and a tilted character after the branch points. The change in character is consistent with the deeper penetrations of free-stream fluid along the upper edge of the $r = 20$ jet than the $r = 10$ jet.

The results presented in this study are presumed valid for $r = 10$ to $r = 25$. The transverse jet is a flow-field that has shown different regimes; in fact the $r = 5$ jet is believed to be in a different regime, where wall effects (image vortices) are important. As a final note and as a practical result, creating a transverse jet flow field that is symmetric about $z = 0$ is not regularly accomplished in laboratory studies, thus determination of the ultimate symmetry or asymmetry of the transverse jet is an open question.

This work was supported by GRI contract # 5093–260–2697, R. V. Serauskas, technical monitor. S. H. Smith was sponsored by the NDSEG fellowship from 1991 to 1993. This work would not have been possible without the diagnostic expertise of R. K. Hanson, and the continued input of E. F. Hasselbrink. Encouragement from J. E. Broadwell was also appreciated.

## REFERENCES

Andreopoulos, J. & Rodi, W. 1984 Experimental investigation of jets in a crossflow. *J. Fluid Mech.* **138**, 93–127.

Broadwell, J. E. & Breidenthal, R. E. 1982 A simple model of mixing and chemical reaction in a turbulent mixing layer. *J. Fluid Mech.* **125**, 397–410.

Broadwell, J. E. & Breidenthal, R. E. 1984 Structure and mixing of a transverse jet in incompressible flow. *J. Fluid Mech.* **148**, 405–412.

Brzustowski, T. A. 1977 Hydrocarbon turbulent diffusion flame in subsonic cross flow. *AIAA Paper* 77-22.

Chassaing, P., George, J., Claria, A. & Sananes, F. 1974 Physical characteristics of subsonic jets in a cross-stream. *J. Fluid Mech.* **62**, 41–64.

Clemens, N. T. 1991 An experimental investigation of scalar mixing in supersonic turbulent shear layers. PhD thesis, Stanford University.

Clemens, N. T. & Mungal M. G. 1995 Large-scale structure and entrainment in the supersonic mixing layer. *J. Fluid Mech.* **284**, 171–216.

Coehlo, S. L. V. & Hunt, J. C. R. 1989 The dynamics of the near field of strong jets in crossflows. *J. Fluid Mech.* **200**, 95–120.

Cohn, R. K. & Koochesfahani, M. 1993 Effect of boundary conditions on axial flow in a concentrated vortex core. *Phys. Fluids* A **5**, 280–282.

Crabb, D., Durão, D. F. G. & Whitelaw, J. H. 1981 A round jet normal to a crossflow. *Trans. ASME* I: *J. Fluids Engng* **103**, 142–153.

Crawford, M. E. & Kays, W. M. 1976 STAN5-A program for numerical computation of two-dimensional internal and external boundary layer flows. *NASA* CR-2742.

Dowling, D. R. & Dimotakis, P. E. 1990 Similarity of the concentration field of gas-phase turbulent jets. *J. Fluid Mech.* **78**, 109–141.

Eckbreth, A. C. 1988 *Laser Diagnostics for Combustion Temperature and Species.* Abacus.

Eiff, O. S. 1996 Experimental analysis of the coherent structures within a turbulent jet in a crossflow. PhD thesis, University of Toronto.

Eiff, O. S., Kawall, J. G. & Keffer, J. F. 1995 Lock-in of vortices in the wake of an elevated round turbulent jet in a crossflow. *Exps. Fluids* **19**, 203–213.

Fearn, R. & Weston, R. P. 1974 Vorticity associated with a jet in a cross flow. *AIAA J.* **12**, 1666–1671.

Fric, T. F. & Roshko, A. 1994 Vortical structure in the wake of a transverse jet. *J. Fluid Mech.* **279**, 1–47.

Haniu, H. & Ramaprian, B. R. 1989 Studies on two-dimensional curved nonbuoyant jets in cross flow. *Trans. ASME* I: *J. Fluids Engng* **111**, 78–86.

Hanson, R. K. 1988 Planar laser-induced fluorescence imaging. *J. Quant. Spectrosc. Radiat. Transfer* **40**, 343–362.

Hasselbrink, E. F. & Mungal, M. G. 1996 An analysis of the time-averaged far-field properties of the transverse jet. *AIAA Paper* 96-0201.

Kamotani, Y. & Greber, I. 1972 Experiments on a turbulent jet in a cross flow. *AIAA J.* **10**, 1425–1429.

Karasso, P. S. 1994 Experiments on mixing and reaction in plane and curved shear layers. PhD thesis, Stanford University.

Karasso, P. S. & Mungal M. G. 1996 Scalar mixing and reaction in plane liquid shear layers. *J. Fluid Mech.* **323**, 23–63.

Keffer, J. F. & Baines, W. D. 1963 The round turbulent jet in a cross-wind. *J. Fluid Mech.* **15**, 481–496.

Kelso, R. M., Lim, T. T. & Perry, A. E. 1996 An experimental study of round jets in cross-flow. *J. Fluid Mech.* **306**, 111–144.

Kelso, R. M. & Smits, A. J. 1995 Horseshoe vortex systems resulting from the interaction between a laminar boundary layer and a transverse jet. *Phys. Fluids* A **7**, 153–158.

Kim, S. W. & Benson, T. J. 1992 Calculation of a circular jet in crossflow with a multiple-time-scale turbulence model. *Intl J. Heat Mass Transfer* **35**, 2357–2365.

Krothapalli, A., Lourenco, L. & Buchlin, J. M. 1990 Separated flow upstream of a jet in a crossflow. *AIAA J.* **28**, 414–420.

Kuzo, D. M. 1995 An experimental study of the turbulent transverse jet. PhD thesis, California Institute of Technology.

Liepmann, D. & Gharib, M. 1992 The role of streamwise vorticity in the near–field entrainment of round jets. *J. Fluid Mech.* **245**, 643–668.

Liscinsky, D. S., True, B. & Holdeman, J. D. 1996 Crossflow mixing of noncircular jets. *J. Propulsion Power* **12**, 225–230.

Lozano, A., Smith, S. H., Mungal, M. G. & Hanson, R. K. 1993 Concentration measurements in a transverse jet by planar laser-induced fluorescence of acetone. *AIAA J.* **32**, 218–221.

Lozano, A., Yip, B. & Hanson, R. K. 1992 Acetone: a tracer for concentration measurements in gaseous flows by planar laser-induced fluorescence. *Exps. Fluids* **13**, 369–376.

McCann, G. J. & Bowersox, R. D. W. 1996 Experimental investigation of supersonic gaseous injection into a supersonic free stream. *AIAA Paper* 96-0197.

McMahon, H. M., Hester, D. D. & Palfery, J. G. 1971 Vortex shedding from a turbulent jet in a cross-wind. *J. Fluid Mech.* **48**, 73–80.

Margason, R. J. 1993 Fifty years of jet in cross flow research. *AGARD-CP* 534, Paper 1.

Moussa, Z. M., Trischka, J. W. & Eskinazi, S. 1977 The near field in the mixing of a round jet with a cross-stream. *J. Fluid Mech.* **80**, 49–80.

Needham, D. J., Riley, N. & Smith, J. H. B. 1988 A jet in crossflow. *J. Fluid Mech.* **188**, 159–184.

Patrick, M. A. 1967 Experimental investigation of the mixing and penetration of a round turbulent jet injected perpendicularly into a transverse stream. *J. Hydronaut. Div. ASCE* **45**, 16–31.

Pratte, B. D. & Baines, W. D. 1967 Profiles of the round turbulent jet in a cross flow. *J. Hydronaut. Div. ASCE* **92**, 53–64.

Shen, G. X. 1991 An experimental investigation in a water channel for the vectoring rectangular jet flows. In *Separated Flows and Jets, IUTAM Symp. Novosibirsk/USSR 1990* (ed. V V. Kozlov & A. V. Dovgal), pp. 863–867. Springer.

Sherif, S. A. & Pletcher, R. H. 1991 Jet-wake thermal characteristics of heated turbulent jets in crossflow. *J. Thermophysics* **5**, 181–191.

Smith, S. H. 1996 The scalar concentration field of the axisymmetric jet in crossflow. PhD thesis, Stanford University.

Sykes, R. I., Lewellen, W. S. & Parker, S. F. 1986 On the vorticity dynamics of a turbulent jet in a crossflow. *J. Fluid Mech.* **168**, 393–413.